Behaviour of buried continuous pipelines crossing strike-slip faults: Experimental and numerical study

Hasan Emre Demirci [a,*], Mustafa Karaman [b], Subhamoy Bhattacharya [c]

[a] *Civil Engineering Department, Izmir Katip Celebi University, Turkey*
[b] *Civil Engineering Department, Izmir Institute of Technology, Turkey*
[c] *Chair in Geomechanics, Civil and Environmental Engineering, University of Surrey, UK*

A B S T R A C T

The paper examines the behaviour of buried continuous pipelines crossing strike-slip faults using experimental and numerical modelling. A newly developed experiment setup is presented along with the derivation of relevant scaling laws and non-dimensional terms governing global response of continuous pipelines to strike-slip faulting. Four model tests are carried out to understand the performance of the pipelines and the results are presented through the derived non-dimensional framework. Three-dimensional (3D) Finite Element (FE) model is also undertaken to simulate buried continuous pipelines crossing strike-slip faults and is calibrated against the model test results and a field case record for validation and verification. A parametric study is also carried out to better understand the parameters influencing the response of buried continuous pipelines to strike-slip faults and to also investigate the effects of pipe end conditions on their behaviour. API 5 L X70 steel pipe with 490 MPa of yield strength was used in the numerical parametric study. Two different scenarios based on fault crossing angle of the pipe (β) were considered in the parametric study: (a) pipelines in tension and bending; (b) pipelines in compression and bending. The experimental and numerical results show that the longitudinal pipe strains under strike-slip faulting are strongly dependent on six parameters: (a) normalized fault displacements (represented by δ/D where δ is the fault displacement and D is the pipe diameter which is also an indication of soil strain in the mobilised zone); (b) ratio of pipe diameter to wall thickness (D/t); (c) fault crossing angle of the pipe (β); (d) relative soil-pipe stiffness (kD^4/EI); (e) ratio of burial depth to pipe diameter (H/D) and (f) pipe end conditions. Finally, practical implications of the study are discussed.

1. Introduction

Pipelines are one of the convenient ways to carry oil, natural gas and water. These commodities conveyed by pipelines are essential to run a nation's industry and economy. Therefore, pipelines are commonly referred to as lifelines since they play a significant role in industries, societies, and economies. It is essential that they remain operational at all times even after a natural disaster such as earthquakes. Pipelines are geographically distributed systems since they are located over large regions often criss-crossing continents and seismic faults. They are normally buried below ground for economic, aesthetic, environmental and safety reasons. Since they are buried below ground, they are supported by a wide variety of soil profiles and need to withstand earthquake related effects in seismic areas.

In seismic areas, pipelines are often subjected to seismic hazards such as faulting, landslides, lateral spreading and effects due to liquefaction. Past earthquake-related damages clearly demonstrated the vulnerability of pipelines to Peak Ground Displacement (PGD), see for instance, pipeline damage which includes local buckling, beam buckling and tensile failure. These are recorded in the aftermath of most recent earthquakes such as 1999 Kocaeli (Turkey), 1999 Duzce (Turkey), 1999 Chi Chi (Taiwan), 2008 Wenchuan (China), 2009 Italy, 2010 Chile and are well-documented in EERI reports (EERI, 2008; EEFIT, 2009; EERI, 2010) and Nair et al. (2018). A quantitative analysis of some of the failures is carried out in Demirci et al. (2018) where several non-dimensional groups are derived. This is therefore an ongoing research issue and physical model tests and numerical modelling are the ways of studying the problem.

Physical modelling (1-g tests in laboratory scale, small scale centrifuge tests, large scale tests) is one of the ways to study behaviour of

---

pipelines crossing active faults and such tests results are scarce in the public domain. This paper reports a series of high quality small-scale physical model tests carried out at 1-g to investigate response of pipelines to strike-slip faulting. The various difficulties in modelling such problem in 1 g is well known and the most important one is the stress level and non-linear behaviour of soils. The approach taken in this study is based on the method suggested in Bhattacharya et al. (2021) whereby the governing equation of the problem is written first and the non-dimensional groups pertaining to the problem is derived from the equation as well as using Buckingham Pi theorem. These non-dimensional groups have a physical meaning and the relevance are verified and validated through numerical modelling as well as experimental modelling. This step provides a convergence of understanding and according to the knowledge of the authors, this type of *Mechanics-based scaling* is the first of its kind in pipeline discipline. Once the identified non-dimensional groups are proved to be reliable, practical range of such values are identified for further investigation and development of useful design charts.

The paper is structured in the following way: A brief literature review is reported to summarise the major contribution in this field and is also presented in Table 1. Section 2 derives the governing equation for the problem together with the physically meaningful non-dimensional groups and similitude relationships. This step is vital for developing physical model tests and this section also provides the description of the experimental set up. Section 3 discusses the tests results and Section 4 verifies and validates the numerical modelling using the experimental results. Section 5 presents the validation of the numerical model through the simulation of a field case record of a failed pipeline in the aftermath of the 1999 Kocaeli Earthquake. Finally, Section 6 presents the parametric study to show the influence of different non-dimensional groups.

1.1. Literature review

1.1.1. Experimental studies

A large body of research including experimental and numerical were carried out in the past two decades to investigate pipeline performance under faulting. O'Rourke and Bonneau (2007) performed large-scale experiments to investigate the performance of steel gas distribution pipelines with 90° elbows and the effects of strike-slip faulting on the behaviour of High-Density Polyethylene (HDPE) pipelines. Abdoun et al. (2009) performed five pairs of centrifuge tests in order to study the effects of various factors on the behaviour of buried HDPE pipes crossing strike-slip faults. The factors considered in their study were soil moisture content, fault offset rate, relative burial depth (H/D) and pipe diameter. Ha et al. (2010) performed a centrifuge test to simulate a failed pipeline behaviour in the 1999 Izmit Earthquake and studied the effects of fault crossing angle (β) on the response of buried HDPE pipelines crossing strike-slip faults. Sim et al. (2012) designed a new testing apparatus which was connected to the shaking table in order to simulate faulting and seismic horizontal shaking simultaneously.

1.1.2. Numerical studies

Vazouras et al. (2010) investigated the mechanical behaviour of buried steel pipelines crossing strike-slip faults considering various steel types and the ratio of pipe diameter to wall thickness (D/t) through numerical modelling. Furthermore, Vazouras et al. (2012) extended their studies to investigate the effects of fault crossing angles (β) on pipeline response to strike-slip faulting and the effects of ovalization, local buckling and tensile failure were reported. In 2015 studies, Vazouras et al. (2015) also studied the effects of pipe end boundary conditions on the behaviour of buried continuous pipelines crossing strike-slip faults. The reported study developed a closed form solution for buried continuous pipelines subjected to pure tension in order to obtain force-displacement relationships at pipe end boundaries. A simplified formulation was proposed by considering various pipe end conditions to predict the occurrence of local buckling.

Table 1
Summary of experimental and numerical works and their key findings.

Research	Type of Study	Fault Type	Key Findings of the Research
O'Rourke and Bonneau (2007)	Experimental Study	Strike-Slip Fault	(1) Pipelines buried in partially saturated soils experienced larger strains than those buried in dry sands. (2) High Density Polyethylene (HDPE) pipelines are ductile and flexible to withstand a significant amount of fault displacements.
Abdoun et al. (2009)	Experimental Study	Strike-Slip Fault	(1) Soil moisture content and fault offset rate did not have a significant influence on the locations and magnitudes of the peak pipe strains. (2) The ratio of pipe burial depth to pipe diameter (H/D) significantly affected magnitudes and locations of peak pipe strains. (3) The peak lateral soil reaction forces acting on the pipes measured in the experiments were in good agreement with the values suggested in the ASCE Guidelines (ASCE, 1984)
Ha et al. (2010)	Experimental Study	Strike-Slip Fault	(1) Placing pipelines with a fault crossing angle of 90° was suggested to minimise longitudinal pipe strains under faulting. (2) High Density Polyethylene (HDPE) pipelines showed a good performance under strike-slip faulting thanks to their high flexibility and ductility.
Sim et al. (2012)	Experimental Study	Strike-Slip Fault	(1) Simultaneous faulting and seismic shaking reduced the shear strength of the soil surrounding the pipe that resulted in the reduction in pipe strains. (2) Bending moments developing within pipelines reduced as fault crossing angle decreased from 90° to lower values. (3) The increase in the relative density of the soil surrounding the pipe resulted in larger pipe strains under faulting.
Vazouras et al. (2010)	Numerical Study	Strike-Slip Fault	(1) Pipelines buried in softer soils such as loose sands and soft clays showed better performance under faulting than those buried in stiffer soils such as dense sands and stiff clays. (2) Pipe internal pressure reduced pipeline performance due to early yielding of the pipe material. (3) Upgrading the steel grade of pipe materials and using thick-walled pipelines increased the performance

(continued on next page)

Table 1 (*continued*)

Research	Type of Study	Fault Type	Key Findings of the Research
Vazouras et al. (2012)	Numerical Study	Strike-Slip Fault	of buried pipelines crossing strike-slip faults. (1) Local buckling is the governing failure mode for buried pipelines subjected to compression and bending forces. (2) Governing performance criteria for buried pipelines subjected to tension and bending are tensile failure and ovalization. (3) The presence of internal pipe pressure increased the ovalization performance of buried pipelines crossing strike-slip faults.
Vazouras et al. (2015)	Numerical Study	Strike-Slip Faults	(1) Prediction of axial pipe strains and pipe displacements by using the proposed closed-form nonlinear force-displacement relationships for buried pipelines in tension showed good agreement with the results obtained from advanced numerical models. (2) Placing a pipeline with a positive value of fault crossing angle that is large enough to avoid local buckling was suggested. (3) The maximum ovalization and axial strains occurred at the buckled pipe cross-section.
Liu et al. (2016)	Numerical Study	Reverse Fault	(1) Upgrading steel grade of pipe materials increased the pipeline performance in terms of local buckling. (2) Upgrading steel grade of pipe materials was recommended to increase pipeline performance under reverse faulting.
Ozcebe et al. (2017)	Numerical Study	Normal Fault	The worst conditions for buried pipelines crossing normal faults in terms of pipe strains developed in two scenarios: a) for large temperature variations and, b) for large values of friction angle at the soil-pipe interface.
Banushi et al. (2018)	Numerical Study	Strike-Slip Fault	(1) Increasing internal pipe pressure diminished the pipeline performance under increasing fault displacements. (2) The radial expansion due to increasing internal pipe pressure resulted in the intensification of the soil-pipe interaction in radial and axial directions. Consequently, this intensification of the soil surrounding pipelines imposes larger soil forces on pipelines under faulting.
Demirci et al. (2018)	Experimental and Numerical Study	Reverse Fault	(1) Pipelines were suggested to be buried at shallow depths at fault crossings in order to reduce pipe strains under reverse faulting.

Table 1 (*continued*)

Research	Type of Study	Fault Type	Key Findings of the Research
			(2) Initiation of local buckling in the pipe wall developed at relatively small fault displacements and significant tensile strains occurred at the buckled area due to folding of the pipe wall. (3) Pipelines were suggested to be buried in softer soils at fault crossings in order to increase pipeline performance under faulting.

Liu et al. (2016) and Demirci et al. (2018) numerically studied the pipeline response to reverse faulting. In the work of Liu et al. (2016), the effects of yield strength and strain hardening parameters of the pipe material on the buckling behaviour of pipelines were investigated. Demirci et al. (2018) numerically modelled experimental results and simulated a field pipeline subjected to a reverse fault. Ozcebe et al. (2017) developed a numerical model to simulate the response of pressurized large diameter buried gas pipelines crossing normal faults and considered cross-sectional buckling and ovalization. Parametric study was also conducted to study the effects of various fault crossing angles (β), properties of soil-pipe interface and operational conditions such as internal pipe pressure and temperature variations on buried pipelines crossing normal faults. Banushi et al. (2018) performed a parametric study to investigate the behaviour of buried continuous pipelines crossing strike-slip faults. A new technique called submodelling technique was proposed to capture behaviour of pipelines at the pipe sections prone to local buckling. The performance of buried continuous pipelines crossing strike-slip faults in terms of tensile strain, ovalization and local buckling was assessed under various parameters including pipe internal pressure and fault crossing angle.

A table summarising the major numerical and experimental works and their key findings is given in Table 1.

2. Experimental modelling

Pipelines crossing strike-slip faults can be modelled as a beam on elastic foundation and steel pipelines generally have relatively small cross-section areas compared to distance between support points. Therefore, Euler-Bernoulli beam approach can be used to model these slender pipelines. A Euler-Bernoulli beam resting on uniform elastic support is demonstrated in Fig. 1. The soil medium surrounding pipelines is assumed to be uniform. Then, the governing differential equation of the problem is very similar to the laterally loaded beam on elastic soil medium. Using the governing equation of the problem, non-dimensional terms can be obtained as in the study of Demirci et al. (2018):

$$\frac{d^4z(\xi)}{d\xi^4} + \left(\frac{P_x D^2}{EI}\right)\frac{d^2z(\xi)}{d\xi^2} - \left(\frac{f(x)D^3}{EI}\right)\frac{dz(\xi)}{d\xi} + \left(\frac{kD^4}{EI}\right)z(\xi) = F \qquad (1)$$

where *EI* is bending stiffness of the pipe, z is lateral deflection of the pipe, $f(x)$ is the friction per length, k is lateral soil spring stiffness (in compression), P_x is axial force in the pipeline at location x and formulated as $P - \int_0^x f(x)dx$, P is external load on pile/beam head (for pipelines crossing active faults, $P = 0$), F is external loads which may be present at the surface level, D is pipe diameter and ξ is non-dimensional length parameter (x/D).

Table 2 summarises the physical meaning of non-dimensional groups governing pipelines crossing active faults and the values of these non-
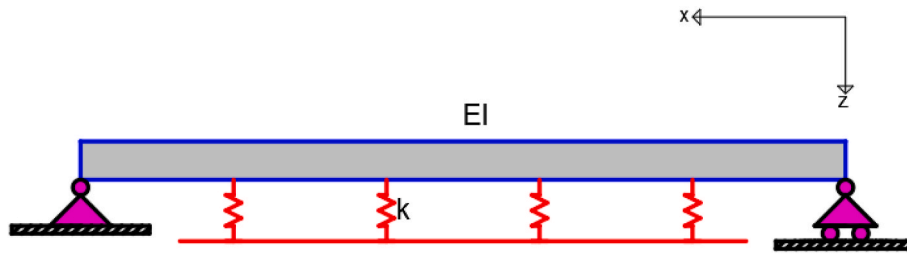
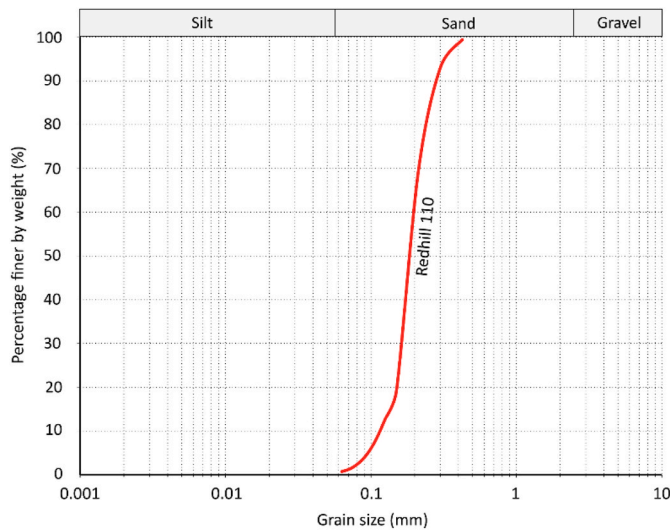**Fig. 1.** A Euler-Bernoulli beam resting on a uniform support.

Fig. 2. Particle size distribution of Redhill 110 sand.

dimensional groups for field and model pipelines are given in Table 3. These non-dimensional groups are obtained via the governing equation and Buckingham π theorem (Rayleigh, 1877; Buckingham, 1914).

2.1. Similitude relationships/scaling laws

Derivation of proper scaling laws and governing non-dimensional terms constitutes the first step in an experimental study. These are essential to have similitude between experimental and field pipelines and to predict the prototype behaviour. The rules of similarity between the model and the prototype that need to be maintained are:

(1) *Scaling of soil:* Grain size effects on soil-pipe interaction cause a significant issue in scaled tests. The backfill material was chosen to ensure that there were no important grain size effects on the response of pipe subjected to Permanent Ground Deformation (PGD). In the literature, the smallest ratio of pipe diameter to average soil grain size (D/D_{50}) was chosen according to the criterion of $D/D_{50} \geq 48$ recommended by the International Technical Committee TC2 (2005) based on centrifuge test data from Ovesen (1981) and Dickin and Leuoy (1983). In addition, the similitude of the ratio between the pipe diameter (D) and the average soil grain size (D_{50}) can also be obtained by applying the result of the investigation of Bolton et al. (1993). The soil used in the experiment is typical Red Hill 110 Silica sand. Relative density of the sand D_r is about 35% which represent the state of loose sand. The engineering properties of Red Hill 110 dry sand is presented in Table 4 and the grain size distribution of the Red Hill 110 sand is shown in Fig. 2.

(2) *Scaling of pipe dimensions (D, t) and burial depth (H):* Pipelines crossing strike-slip faults are one of the examples of soil-structure
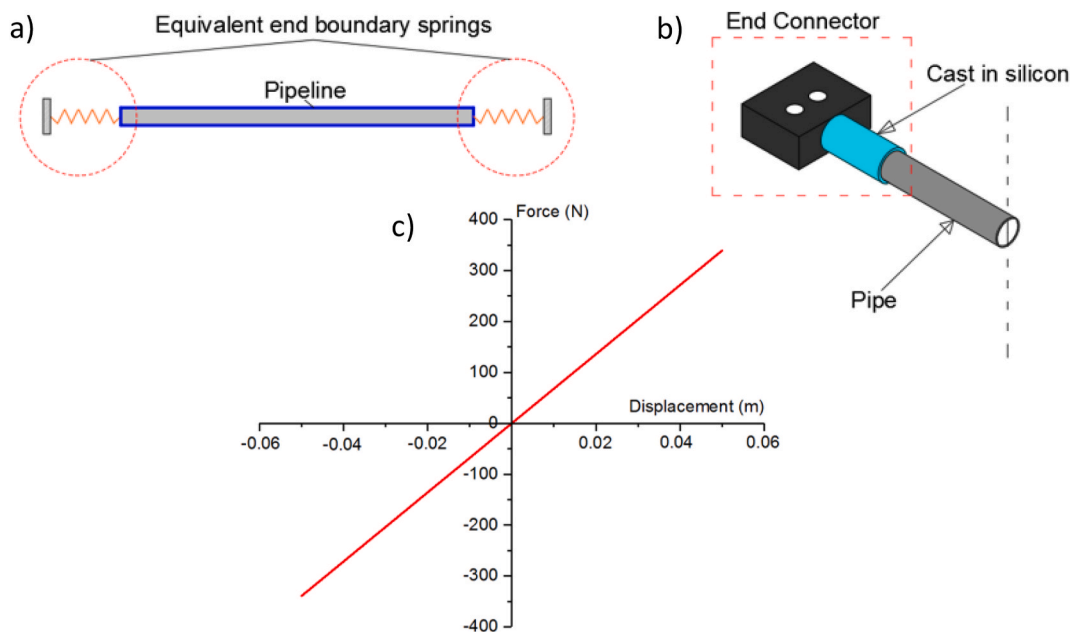

Fig. 3. a) The schematic sketch of end connection springs, b) details of pipe-end connection, and c) force-displacement relationships of the material of the end connector.

Table 2
Scaling laws for studying soil-pipe interaction under faulting.

Name of the non-dimensional group	Physical Meaning	Remarks
$\left(\dfrac{kD^4}{EI}\right)$	Flexibility of the pipeline so as to have similar soil-structure interaction	Small (kD⁴/EI): rigid pipe behaviour Large (kD⁴/EI): flexible pipe behaviour
$\left(\dfrac{D}{t}\right)$	Slenderness of the pipeline (affects pipeline failure mode)	Large (D/t): shell buckling failure mode Small (D/t): beam buckling failure mode
$\left(\dfrac{H}{D}\right)$	Non-dimensional burial depth (affects soil failure type)	Small (H/D): wedge type of soil failure Large (H/D): soil flow around the pipe
$\left(\dfrac{p}{\sigma_y}\right)$	Non-dimensional pipe pressure	The change in Hoop stress (This will influence the pipeline behaviour under faulting)
$\left(\dfrac{\delta}{D}\right)$	Non-dimensional fault displacement (strain field in the soil around the pipeline)	Similar strain field will control soil-pipe interaction
β	Fault Crossing Angle	β: compression + bending - β: tension + bending

Table 3
Values of non-dimensional groups for field and model pipelines.

Non-dimensional group	Field (prototype) values (Range)	Model values (Range)	References
$\left(\dfrac{kD^4}{EI}\right)$	0.03–0.13	0.06–0.09	SGC (1973), Schiff et al. (1998) and Ha et al. (2008)
$\left(\dfrac{D}{t}\right)$	72.4–125	16.67	(1971 San Fernando Earthquake, 1999 Chi Chi Earthquake, 1999 Kocaeli Earthquake)
$\left(\dfrac{H}{D}\right)$	1.4–4	5–7	
$\left(\dfrac{\delta}{D}\right)$	1.4–5	1–6	
β	−90° < β < +90°	−75°, +75°, 90°	
$\left(\dfrac{p}{\sigma_y}\right)$	0.008–0.11 (maximum operating pressure is considered)	Not considered in this study.	ASME (2006) and ASME (2007)

Table 4
Engineering properties of Red Hill 110 dry sand.

Properties	Values
Specific gravity	2.65
Median particle diameter D_{50} (mm)	0.144
Peak Internal friction angle ϕ_{peak} (deg)	40
Residual internal friction angle ϕ_{cv} (deg)	34
Dry unity weight (kN/m³)	13.0
Maximum void ratio e_{max}	1.035
Minimum void ratio e_{min}	0.608
Relative density D_r %	35

Table 5
Selected pipe characteristics for the experimental study.

Model Test	Pipe Material	Diameter (m)	Wall Thickness (m)	Burial Depth (m)	Fault Crossing Angle (°)	Total Curved Length (m) = 2xL_c	Relative soil-pipe stiffness (kD⁴/EI)
T-1	HDPE	0.05	0.003	0.25	90	1.24	0.06
T-2				0.35		1.1	0.09
T-3					−75		
T-4					75		

interaction problems in geotechnical engineering. The governing non-dimensional parameter for deflection characteristics of such problems is relative soil-pipe stiffness (kD⁴/EI). Lateral spring stiffness (k) is dependent on engineering soil properties such as internal friction angle (ϕ), cohesion (c), unit weight of soil (γ), burial depth of pipe (H) and pipe diameter (D). On the other hand, the pipe characteristics influencing pipe flexural stiffness (EI) are pipe material, diameter (D) and wall thickness (t). As seen in Table 3, kD⁴/EI in the field varies between 0.03 and 0.13 so that this range will be considered for the experimental study. Furthermore, total curved length of the pipeline (2xL_c) should be less than total length of the test set-up, which is 2 m, in order to avoid boundary effects on the bending behaviour of the pipeline. The length over which lateral displacement occurs due to curvature (L_c) is a function of lateral soil force per unit length (P_u), fault movement (δ) and pipe bending stiffness (EI) (Sarvanis and Karamanos, 2017). The pipe diameter (D), pipe wall thickness (t) and pipe burial depth (H) are selected considering both field kD⁴/EI values and the limit value of 2xL_c. Pipe material, diameter, wall thickness and burial depth used in the experimental model are summarised in Table 5. As seen in the table, the values of kD⁴/EI for model pipelines ranges between those values for prototypes summarised in Table 3 and the value of 2xL_c is smaller than the box length (L = 2 m).

(3) *Scaling of the anchorage length:* A sufficient anchorage length of pipe is necessary in order to avoid the boundary effects and simulate real field conditions accurately. Several hundreds of pipe diameter length (L_a/D) are needed to be achieved for required anchorage length (Kennedy et al., 1977). Equivalent boundary method, which is used to obtain force-elongation (F-δ) relationship for end springs (see Liu et al., 2004; Vazouras et al., 2015; Zhang et al., 2016), is used in the study to minimise the boundary effects and to simulate more realistic end conditions than fixed boundaries. In the experimental study, silicon material, which has similar F-δ relationship, is used to simulate end connection springs (Fig. 3a–b). End connectors are designed to simulate axial soil-pipe interaction along the unanchored length, so they are placed out of the curved zones within the pipeline. The end connector has a negligible rotational stiffness, so it only provides axial continuity at pipe ends. Force-displacement relationship of the end connector is plotted in Fig. 3c. More details about the design and construction of the end connector can be found in the work of Demirci (2019).

(4) *Scaling of fault movement:* In order that the fault movement in the experimental model is of a comparable magnitude to real fault movements, the fault displacement is assessed by the ratio of fault displacement to the pipe diameter (δ/D). Fault displacements vary considerably in the field as observed from past earthquakes (Table 3). In this study, horizontal fault movement (δ) is limited to 300 mm, resulting in maximum δ/D of 6.

(5) *Scaling of Offset Rate:* Turner (2004) explored the impact of offset rate on soil-pipe interaction forces by using three different offset rates of 0.03 mm/s, 0.3 mm/s, and 25 mm/s and concluded that the influence is nearly negligible. However, Abdoun et al. (2009) observed that the high-density polyethylene (HDPE) pipe bending strains recorded in the fast offset rate test were almost

always larger than those values recorded in the slow offset rate test. This is consistent with HDPE material properties since HDPE has strain rate dependent behaviour (i.e. softer at lower strain rates). Therefore, offset rate effects on the behaviour of pipelines crossing strike-slip faults should be taken into account. In this study, offset rate of 0.173 m/min is used for the model tests. The fault offset rate in the centrifuge tests (Ha et al., 2008) was 0.32 m/min. The upperbound for the expected prototype offset rate is about 60 m/min. Therefore, the fault offset rate used in this study can be considered as slow compared to the prototype offset rate.

2.2. Test setup

An experimental model has been developed to understand the behaviour of buried continuous pipelines crossing strike-slip faults. The model consists of two identical boxes. One box is fixed whereas other

can move horizontally on bearings and rails. The moveable part is displaced up to 300 mm by an electrical linear actuator. The plates are used at the both side of the model to prevent the soil leaking out of the boxes. The dimensions of the model are 2 m length, 1 m width and 0.75 m depth. Fig. 4a shows isometric sketch of split boxes with their dimensions and Fig. 4b illustrates a photo of the split boxes.

Fig. 5 demonstrates side, front and plan views of the experiment setup with all components of the test setup. Rails and linear bearings were used to guide and support the moving part. This provides accurate movement and minimum friction desired. The rails were bolted on the wood bases. The wood base was used to flatten the surface underneath the rails. The wood base was bolted to the strong floor. The actuator was attached to movable box and it was fixed to strong floor by a bolt. A frame surrounding the actuator was constructed in order to constrain potential rotations of the actuator. The bottom of the fixed box was constrained in any directions by bolting it to the fixed base. The fixed
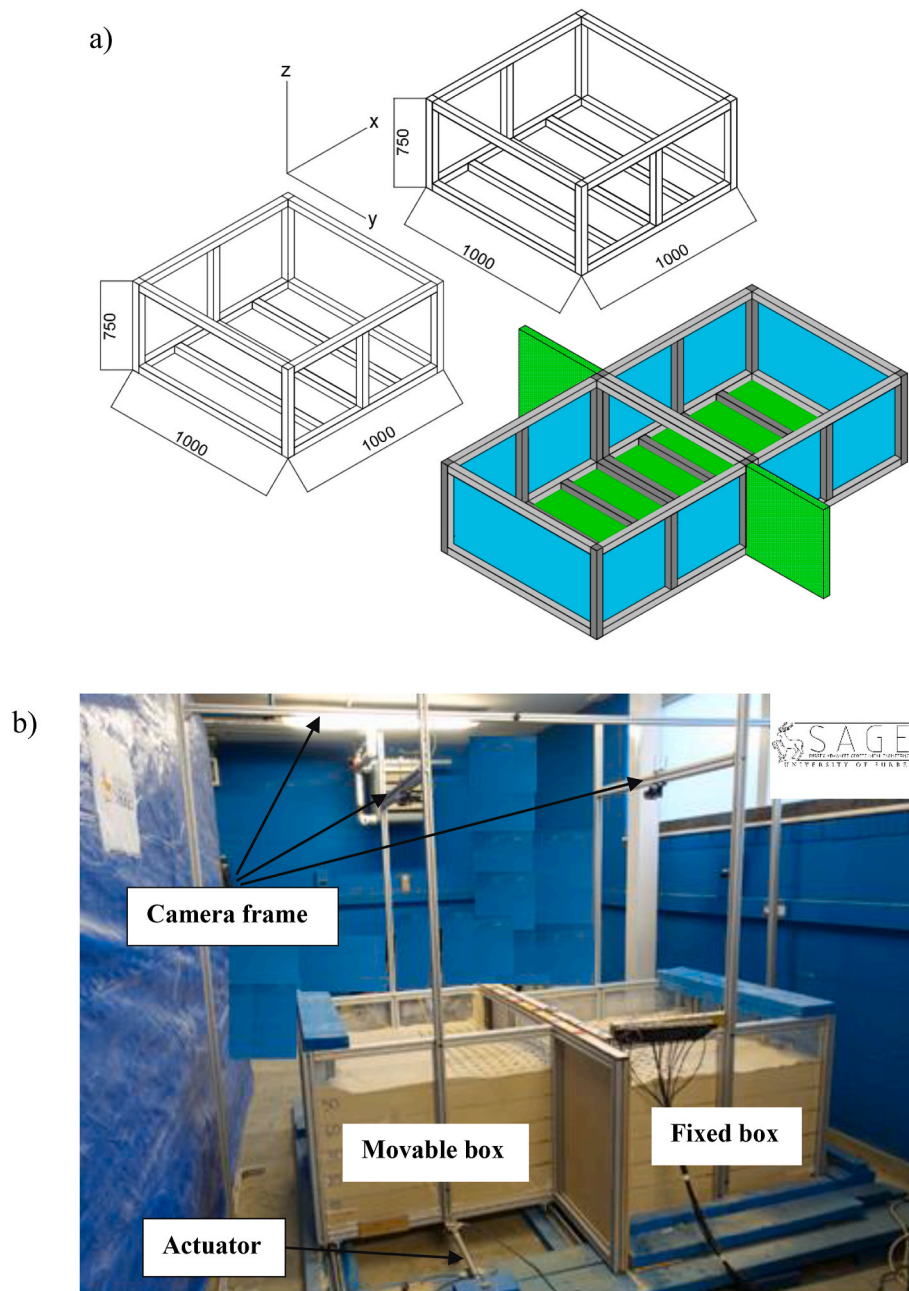

Fig. 4. a) Isometric sketch of the split boxes showing dimensions of them in three directions (all dimensions are in mm) and b) a photo of the split boxes.
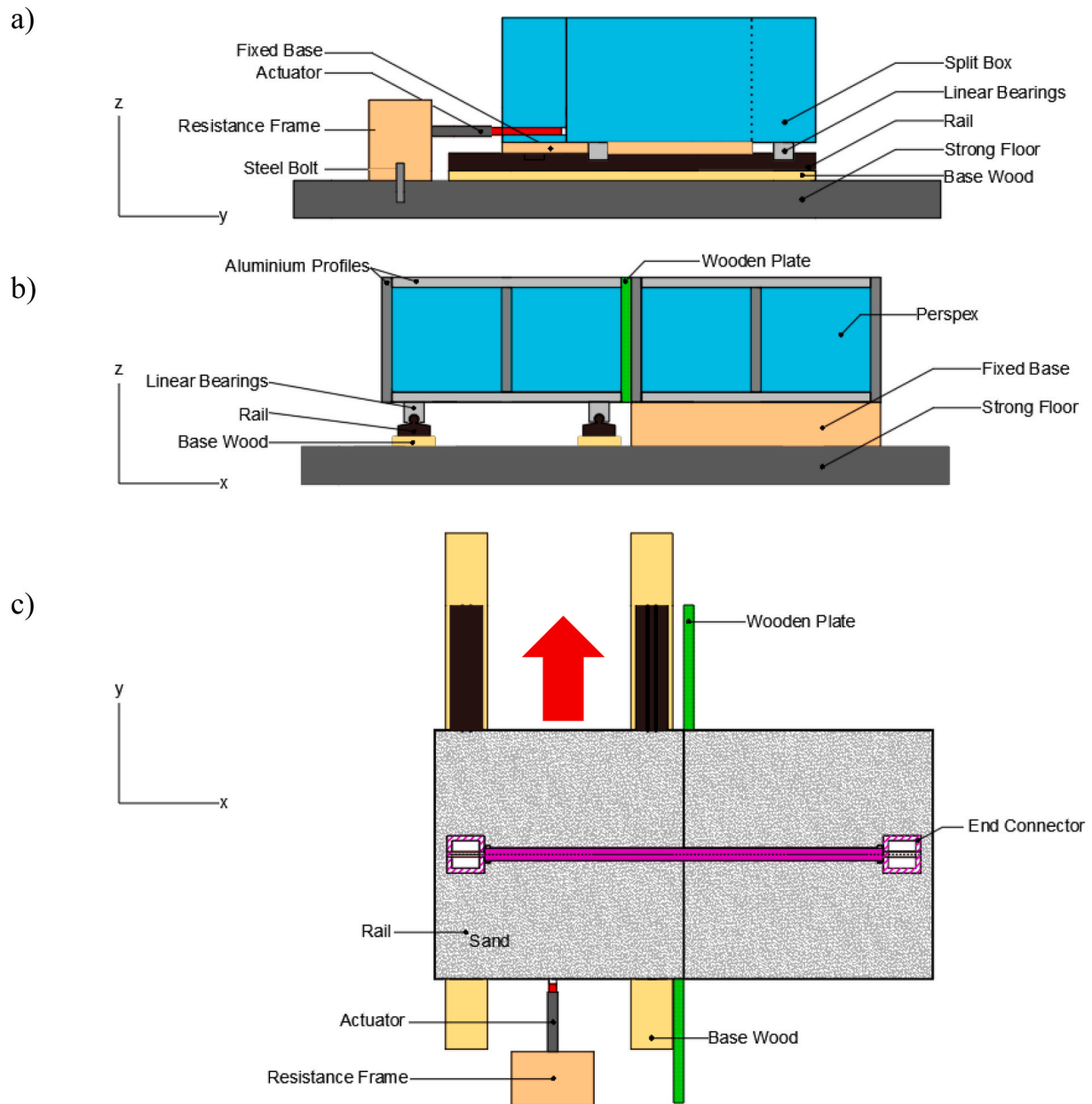
Fig. 5. a) Side view of the experiment setup, b) front view of the experiment setup, and c) plan view of the experiment setup.

base was constructed using wood plates and the plates were bolted to strong floor.

The aluminium alloy struts with 40 × 40 mm cross-section and 8 mm groove were used to construct frame of the split box. The aluminium alloy struts were preferred due to their lightness and strength. Perspex material was used to cover side walls of the split box whereas bottom of the split box was covered by plywood material. The plywood material (shown in Fig. 5 with green colour) was also used to prevent the sand leaking out from the boxes. Polytetrafluoroethylene (PTFE) sheets are glued to the surface of the plywood material in order to decrease friction between the box surfaces. Pipe insulation foams with 40 mm outer diameter were also placed between sliding surfaces to prevent the sand from leaking between the boxes. The pipe insulation foams were compressed to provide tightness at the sliding surfaces. More details about the design and construction of the test setup can be found in the work of Demirci (2019).

As shown in Fig. 6a, six steel bars of 20 mm diameter were fixed on either side of the box. The bars were fixed at the base and also at the top

which was used to connect the end connectors. It is convenient to use steel bars rather than linking the end connectors directly to the box walls since steel bars allow the pipe to be located at any desired depth. Furthermore, model pipes can also be placed with various fault crossing angles (90°, +75°, −75°) using the same steel bars as shown in Fig. 6b.

Three types of instrumentation were used to monitor performance of the model setup and pipeline response to strike-slip faulting. S type beam load cell was used to measure applied load to the movable box to displace it up to desired displacement. The load cell fixed between the actuator and the movable box. The load cell was calibrated against calibrated weights. A laser displacement sensor was used to monitor displacement of the movable box with respect to time. High Density Polyethylene (HDPE) pipes were instrumented with strain gauges along the pipe spring-lines. The strain gauges were used to measure longitudinal strain distribution on the east and west spring-lines. Longitudinal strains are combination of bending and axial strains. Bending strains were calculated as one-half difference between the longitudinal strains at east and west spring-lines while axial strains were calculated as the
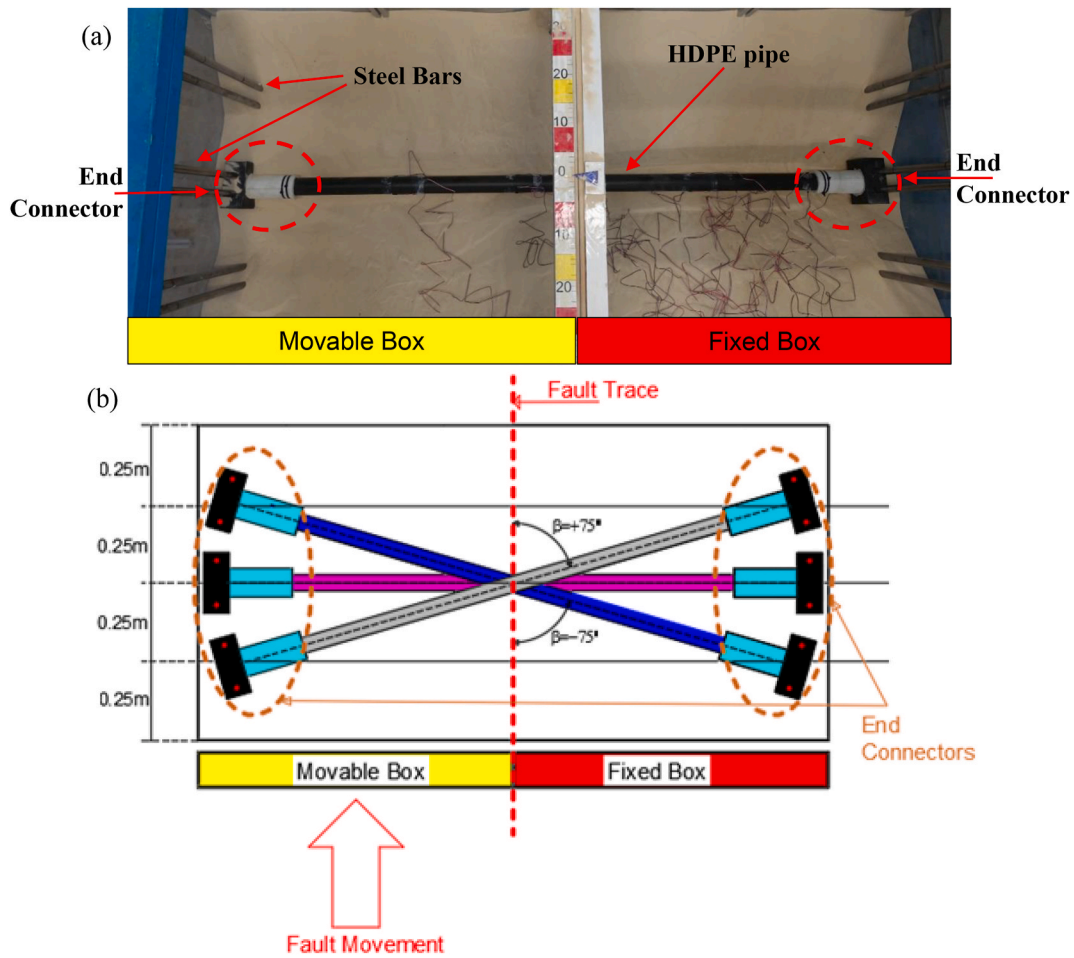
Fig. 6. a) The plan view of the experiment setup showing end connectors and steel bars and b) the plan view of the experiment setup showing the placement of model pipes with various fault crossing angles.

average of the longitudinal strains at spring-lines. Five pairs of strain gauges were placed along the pipes. Two different layouts of strain gauges along the pipeline were used in the tests. The schematic illustrations of strain gauge layouts and pipe spring-lines are shown in Fig. 7a–c.

3. Experiment results

Four model tests were performed to assess the performance of the newly developed model setup of pipelines crossing strike-slip faults. In the model tests, High Density Polyethylene (HDPE) pipes with a diameter of 50 mm and a wall thickness of 3 mm were used. Two different burial depths and three different fault crossing angles were used: (a)

Burial depths of 250 mm and 350 mm, (b) Fault crossing angles of 90°, +75° and −75° were used in the model tests (see Table 5). The experimental plan of the model tests is summarised in Table 6.

Axial strain distributions along the pipeline under various fault displacements for T-1 are demonstrated in Fig. 8. Data points obtained from strain gauges and trend-lines for these points are seen in the figure. The trendlines are polynomial fitted lines for the axial strain data obtained by the experiment. From the previous researches (Ha et al., 2008; Abdoun et al., 2009), it is expected that maximum axial pipe strains develop at about fault trace and axial pipe strains decrease along the pipeline with moving away from the fault trace. Also, symmetrical distribution of pipe axial strains at around the fault trace (for homogeneous soils) is observed from these works. In the light of these observations
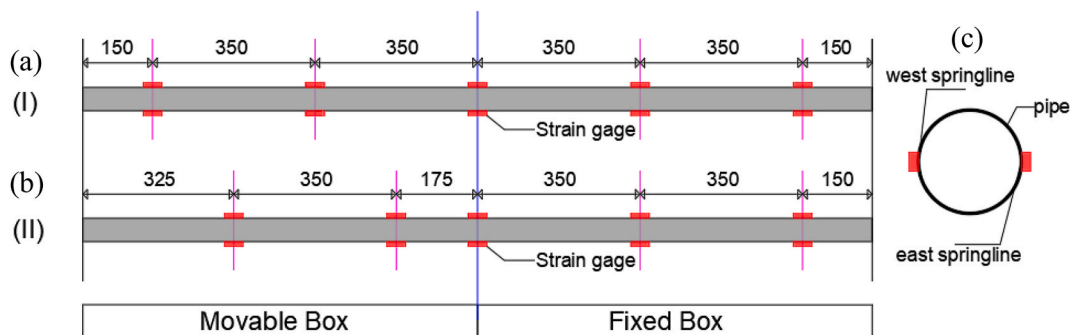

Fig. 7. a) Strain gauge layout I, b) strain gauge layout II and c) pipe spring-lines (All dimensions are in mm).

Table 6
Selected pipe characteristics for the experimental study.

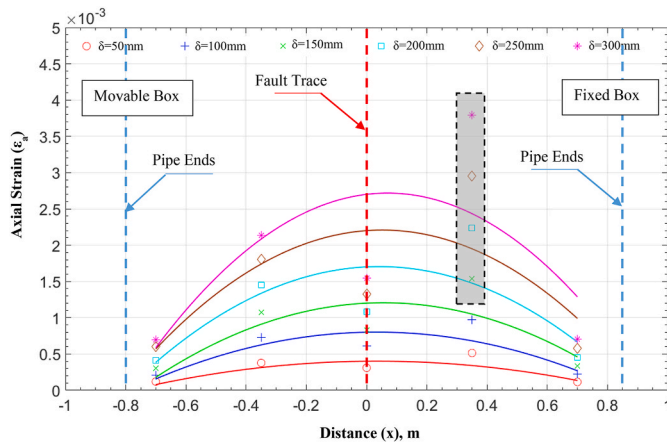| Model Test	(H/D)	(D/t)	$(\delta/D)_{(max)}$	Strain Gauge Layout
T-1	5	16.67	6	I
T-2	7			II
T-3				
T-4				

Fig. 8. Axial strain distribution for T-1.

from the past researches, it is concluded that the axial strains shown in gray-dashed rectangle (Fig. 8) are erroneous values. The error may arise due to some problems associated with strain gauges or some local effects at this location. The magnitude of axial strains measured in the experiments are in order of 10^{-3} (see Fig. 8) while the magnitude of pipe bending strains are in order of 10^{-2} (see Fig. 9). This comparison shows that pipe axial strains are less critical than bending strains at the vicinity of fault crossings. This conclusion is valid for buried pipelines crossing strike-slip faults with a fault crossing angle of 90° and flexible end boundary conditions considered in the experiment. It should be kept in mind that pipe end boundary conditions and fault crossing angles have a significant effect on pipe axial strains.

As observed from axial and bending strain distribution plots, buried continuous pipelines crossing strike-slip faults with 90° of fault crossing angle experienced bending dominated behaviour since bending pipe strains are much larger than axial pipe strains in the curved zone.

The variation of peak bending strains with normalized fault displacements for four model tests is plotted in Fig. 10. Peak bending
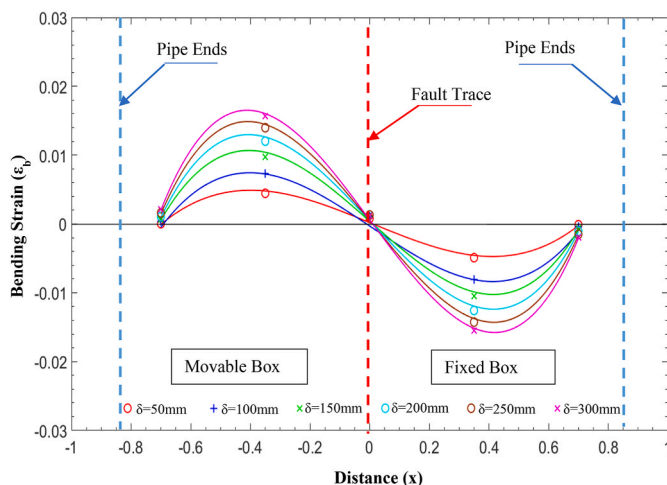
strains show logarithmic growth with the increase in fault displacements. Peak bending strains experience plateau with the increase in fault displacements due to that ultimate lateral soil resistance is reached. Peak bending strains increase with the increase in burial depth (comparison of T-1 and T-2). Fig. 11 shows variation of peak axial strains with normalized fault displacements for four model tests. Peak axial strains increase with increasing burial depth (comparison of T-1 and T-2) and larger peak axial strains occurs at −75° and +75° fault crossings (comparison of T-2 and T-3, T-4).

4. Calibration of the numerical model via experiment results

A three-dimensional (3D) Finite Element (FE) model of experiment T-1 was developed and results of 3D FE analysis were compared to results of T-1 to calibrate the developed 3D FE model. Relevant information of T-1 was shown in Tables 5 and 6. An overview of the model test used for the calibration of the developed numerical model, materials used in the model tests, the strategy followed for the numerical modelling and comparison of numerical results to the test results are presented in following sections.

4.1. Overview of the model test used for the calibration

Fig. 5 shows the model test setup of buried continuous pipelines crossing strike-slip faults and its schematic explanation of the working principle. Table 5 shows the burial depth, pipe material, pipe diameter, pipe wall thickness used in T-1. The engineering properties of Red Hill Sand are given in Table 4. The Young's Modulus of HDPE pipe material and its yield strength were used as 750 MPa and 14 MPa, respectively. The variation of peak friction angle of Red Hill 110 dry sand as a function of mean effective stress and relative density is shown in Fig. 12. Fig. 12 is plotted by using the equation proposed by Bolton (1986) which is shown in Equation (2). Young's modulus of the Red Hill sand at the relative density of 35% was calculated by using shear modulus of the sand at small strains (G_0) value.

$$\phi' = \phi_{cv} + 3[R_D(9.9 - lnp') - 1] \qquad (2)$$

where ϕ_{cv} is residual internal friction angle, R_D is relative density, p' is mean effective stress.

The shear modulus at small strains (G_0) of the sand medium in the test was obtained using the method which is schematically explained in Fig. 13. The distance between the accelerometers is denoted by l. The vibration wave generated by the applied impact load on the side wall of
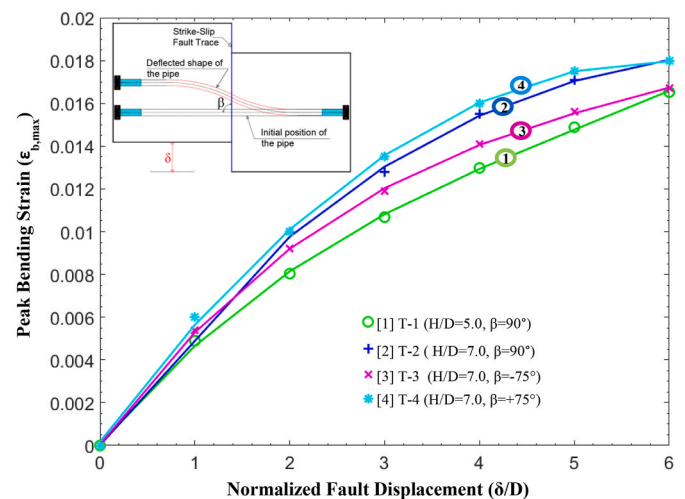

Fig. 9. Bending strain distribution for T-1.

Fig. 10. Peak Bending Strain ($\varepsilon_{b,max}$) vs. Normalized Fault Displacement (δ/D) for model tests.
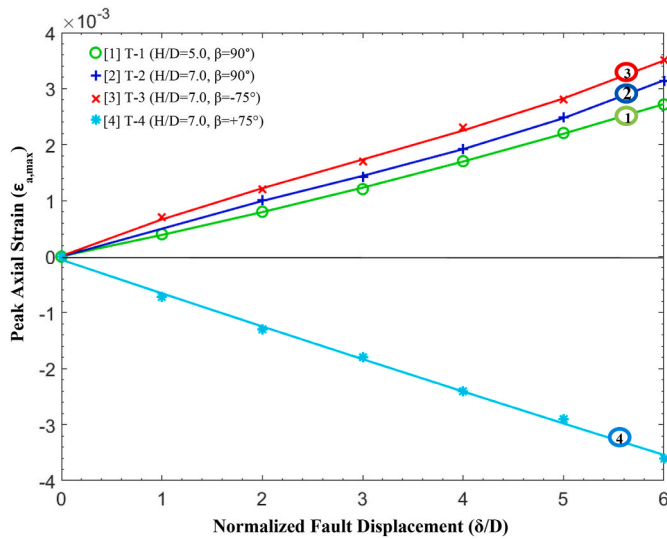
Fig. 11. Peak Axial Strain ($\varepsilon_{a,max}$) vs. Normalized Fault Displacement (δ/D) for model tests.
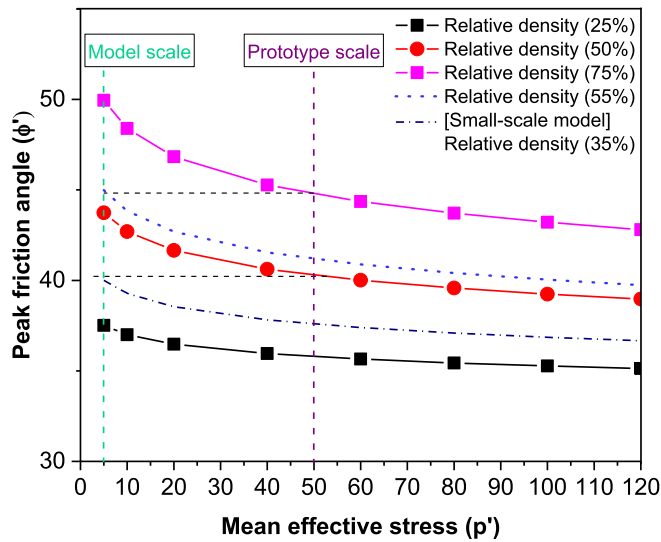

Fig. 12. The variation of peak friction angle of Red Hill 110 dry sand as a function of mean effective stress and relative density.

the box by a hammer will arrive at the accelerometers in sequence and the travel time of the wave between accelerometers (Δt) was recorded. Fig. 13b–c shows the acceleration signals recorded by Acc 1 and Acc 3. The shear modulus at small strains (G_0) of the sand is calculated using Equations (3) and (4).

$$v_s = \frac{l}{\Delta t} \tag{3}$$

$$G_0 = G = \rho_s \Delta v_s^2 \tag{4}$$

where v_s is shear wave velocity and ρ_s is the density of the sand.

The travel time of the wave between Accelerometer 1 (Acc1) and Accelerometer 3 (Acc3) is found as 0.01 s. The distance between Acc1 and Acc3 is 0.6 m as seen in Fig. 13a. Then, the shear wave velocity of the soil (v_s) can be calculated as 60 m/s. Finally, shear modulus at small strain (G_0) is calculated as 5.1 MPa.

4.2. Modelling strategy

The three-dimensional (3D) Finite Element (FE) simulation of T-1 model test was developed by using ABAQUS v 6.14. ABAQUS/Explicit module was utilized to solve this soil-pipe interaction problem under strike-slip faulting (T-1 Test). Two different stages were used to simulate the real model test conditions: (a) gravity loading and (b) fault displacement. Gravity loading was applied to the whole model to simulate the stresses in the soil and on the pipe due to the self-weight of the soil and pipe. In the second step, fault displacement with a 90° fault crossing angle (300 mm displacement in the horizontal direction) was applied incrementally to the left-hand side soil block (movable box) while right-hand side soil block (fixed box) was kept fixed. Continuum elements (C3D8R) were used to model the soil and Mohr-Coulomb constitutive model was chosen to represent the stress-strain relationship in the soil. A standard Mohr-Coulomb model is characterized by the internal friction angle (φ), dilation angle (Ψ) the soil cohesion (c), the elastic modulus (E), and Poisson's ratio (ν). Shell elements were used to model the pipe and the Isotropic Von-Mises yield model was selected to simulate the pipe material. Normal and tangential contacts were used to simulate the interaction between the soil and pipe. The tangential contact algorithm with friction coefficient (μ_f) simulates the friction interaction between the soil and pipe. Normal contact algorithm simulates pressure-overclosure relationships at the soil-pipe interface. Hard contact is an option under normal contact algorithm and it allows separation of the soil and pipe surfaces once they come into contact, see Abaqus Analysis User's Guide (2014). The soil-pipe interface friction coefficient (μ_f) was taken as 0.4 in the numerical model. Two different cases were considered for the FE analysis: (a) peak internal friction angle (φ_{peak}) was used for the Case I and (b) residual internal friction angle (φ_{cv}) was used for the Case II. Red Hill sand at 35% relative density has peak internal friction angle of 40°, residual internal friction angle of 34° and it needs a dilation angle of 6° at this relative density. Young's modulus of the sand (E) is calculated by using the value of G_0 as explained in section 4.1. The stiffness reduction with increasing strain amplitude is not considered in the 3D FE model. This leads to overestimation of pipe strains under small relative soil-pipe movement as the sand has large stiffness that does not reduce under increasing strains. A constant value of the shear modulus was used for each depth. In other words, the stiffness increase with depth was not considered in the numerical model. Ignoring the variation of shear modulus with depth is thought to not affect the pipeline behaviour as it was buried at a constant depth and the value of shear modulus at pipe burial depth was used in the 3D FE model. The soil parameters used in the numerical model for Case I and Case II are shown in Table 7.

The vertical boundary nodes (side walls) of the fixed parts were restricted in the horizontal direction and the bottom wall of the fixed soil block was restricted as an encastre. The uniform fault displacement was applied in the external nodes of the moving part in horizontal (z) direction as in the experimental model (see Fig. 14). Equivalent boundary end springs were connected to each pipe ends to simulate the end connectors that were used in the model tests. The force displacement relationship for the end springs can be seen in Fig. 3c.

A fine mesh was employed for the soil surrounding the pipeline, and the region close to the strike-slip fault trace, where the pipe and fault intersect (see Fig. 14). Maximum stresses and strains in the soil and pipeline are expected to develop in these parts. On the other hand, a coarser mesh is used for the soil parts far from the fault trace (Fig. 14a). The magnitude of the displacements (U) in soil blocks is shown in Fig. 14a. The unit of the displacements in the legend in Fig. 14a is in meters (m). Fig. 14b shows the displacement profile of the pipeline. Fig. 14c shows cross-section of soil continuum model along with the pipe burial depth and cross-section dimensions of the model.
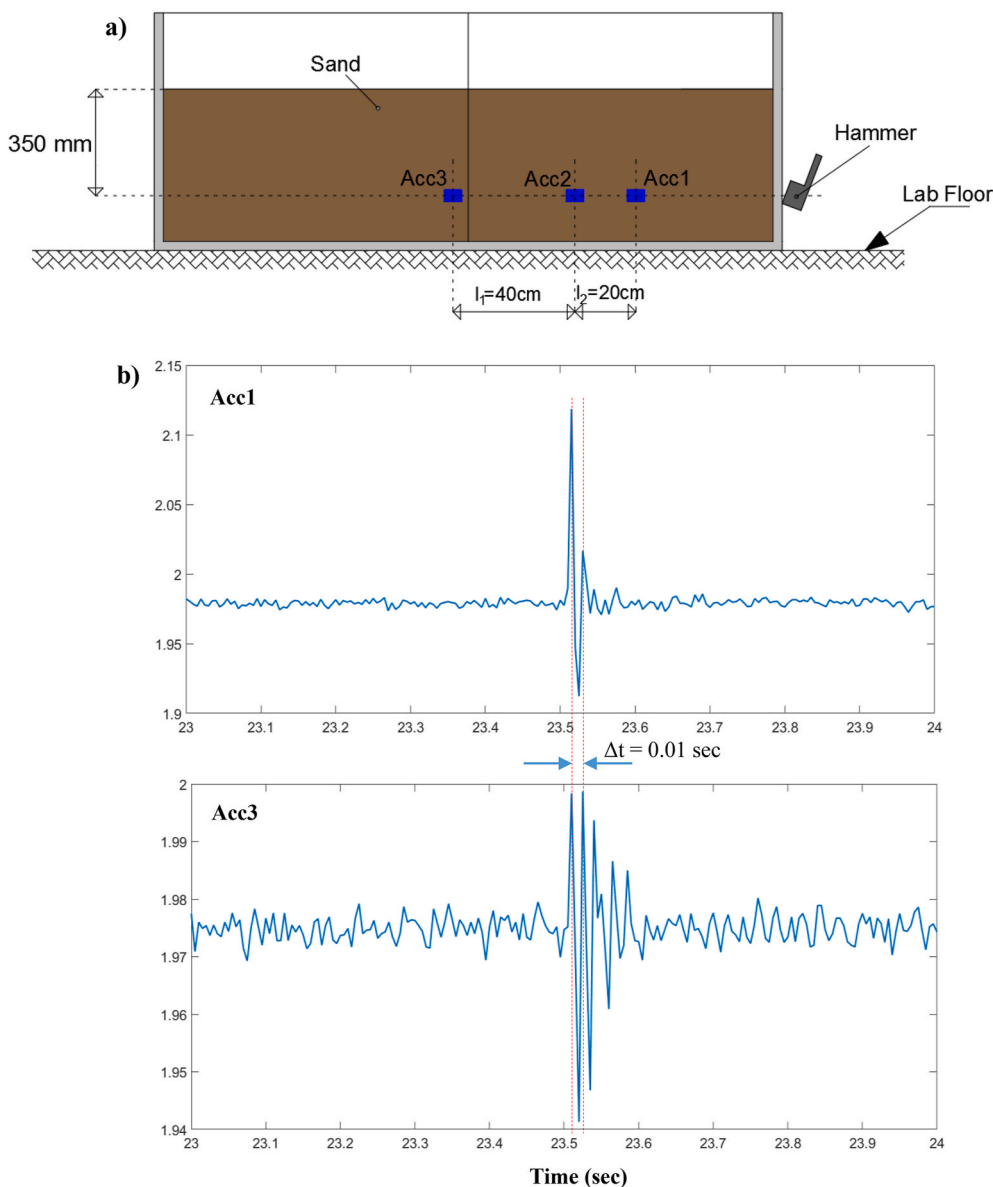
Fig. 13. a) Shear wave velocity method, b) acceleration signals recorded by Acc1 and Acc3.

Table 7
Parameters used in the 3D numerical model for Case I and Case II.

CASE I -Soil: Red Hill Sand			
Elastic		Plastic	
E (MPa)	13	ϕ (°)	40°
ϑ	0.4	Ψ (°)	6°
		c (kPa)	0

CASE II -Soil: Red Hill Sand			
Elastic		*Plastic*	
E (MPa)	13	**ϕ (°)**	34°
ϑ	0.4	**Ψ (°)**	6°
		c (kPa)	0

4.3. Comparison against the model test (T-1)

Fig. 15 plots measured bending strain distribution from T-1 test and calculated bending strain distribution from numerical analysis for Case I and Case II. Black points show the bending strains measured in the model test under a fault displacement of 300 mm ($\delta/D = 6.0$). The red dotted line demonstrated the bending strains that were predicted by numerical analysis under the same fault displacement ($\delta/D = 6.0$) for Case I. The blue dashed line shows the bending strains that were predicted by numerical analysis under $\delta/D = 6.0$ for Case II. The maximum bending strains and their locations observed in the experiments were well predicted by the numerical model for Case II whereas the maximum bending strains were over-predicted by the numerical model for Case I. The pipe bending strains close to the pipe ends (at the locations of -0.7 m and $+0.7$ m where the fault trace is on 0.0 m) were overpredicted by both models for Case I and Case II. Therefore, the numerical models provide conservative estimations of pipe bending strains at these locations. However, the pipe bending strains at locations of -0.7 m and $+0.7$ m are relatively small compared to maximum pipe bending strains measured along the pipeline. The overprediction of bending strains far from the fault crossing is not critical in the sense of the pipeline design since buried pipelines crossing faults are designed considering maximum pipe strains expected along the pipeline. Therefore, the main aim of the numerical models is to predict maximum pipe strains and their locations along the pipelines under faulting. To sum up, the developed model for Case II in which residual internal friction angle was
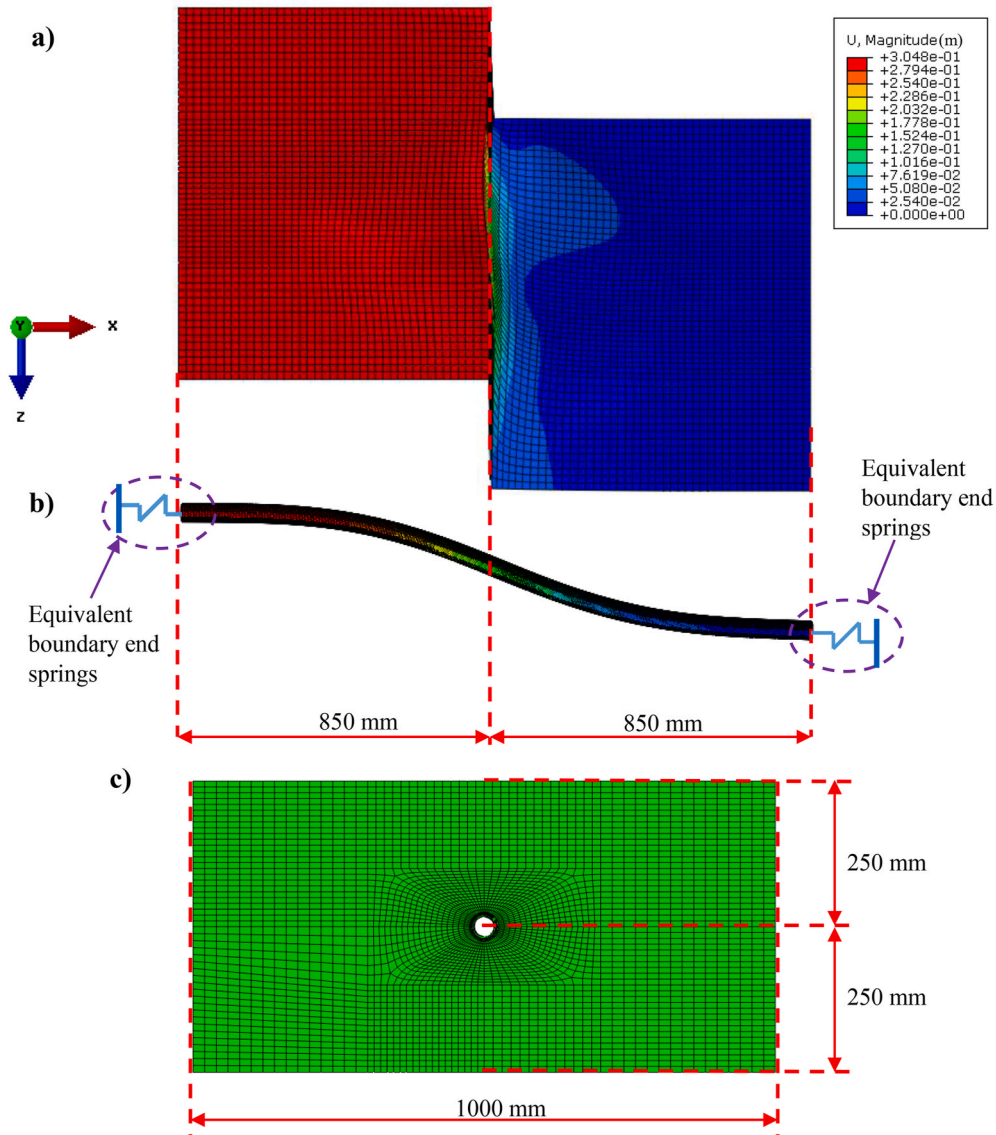
Fig. 14. a) Plan view of the 3D FE model showing displacements of fixed and movable soil blocks, b) displacement profile of the pipeline, and c) cross-section of soil continuum model showing pipe burial depth and cross-section dimensions.
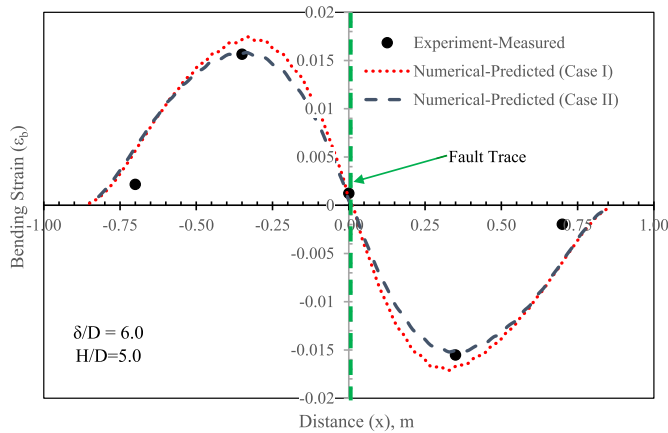

Fig. 15. Plots of pipe bending strains (ε_b) versus distance from the fault (x) for T-1 and numerical analysis.

used in the soil model predicts the maximum bending strains and their locations along the pipeline quite well. The developed numerical model for Case I in which peak internal friction angle was used in the soil model provides conservative estimations of bending strains along the model pipeline.

Fig. 16 shows the plot of peak bending strains versus normalized fault displacements for the experiment and numerical analysis (Case I and Case II). The brown line shows measured bending strains from the experiment whereas blue dashed line (Case II) and red dotted line (Case I) show calculated bending strains from the numerical analysis. For all values of normalized fault displacements (δ/D ranging from 0 to 5), peak bending strains obtained for Case II overestimate the those recorded in the experiment. The values of predicted and recorded peak bending strains are getting closer to each other with increasing normalized fault displacements (δ/D). For all values of δ/D, the predicted peak bending strains in Case I are conservative, which are larger than those recorded in the experiment. The relative density of Red Hill sand used in the experiment is 35% which is considered as a loose state. Loose to medium sands experience dilative behaviour at a low stress level. The soil stress level in the model test is low so that Red Hill sand experience dilative behaviour throughout the experiment. Mohr-Coulomb constitutive
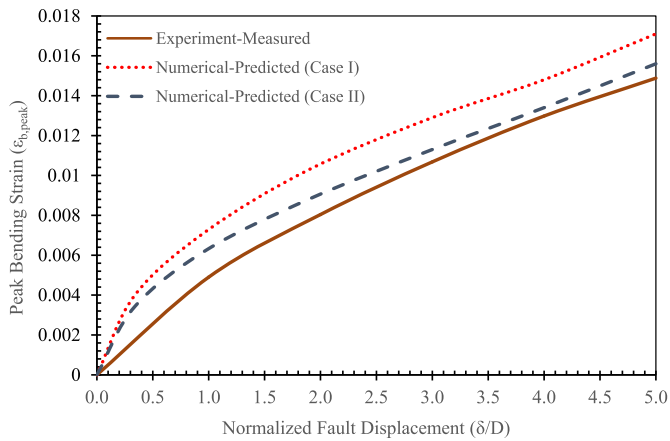
Fig. 16. Plots of peak bending strains ($\varepsilon_{b,peak}$) versus normalized fault displacements (δ/D).

model was used in numerical analysis to simulate stress-strain behaviour of the Red Hill sand surrounding the pipeline. Mohr-Coulomb soil model is an elastic-perfectly plastic model so that it cannot capture strain softening behaviour of the loose sands under low stress levels. Due to that reason, the discrepancy between predicted and measured peak bending strain values are larger at smaller values of δ/D than the discrepancy at larger values of δ/D. The Red Hill sand surrounding the model pipe reached its residual strength under large values of δ/D so that Case II in which residual internal friction angle was used provides better estimation of peak bending strains under large fault displacements. Another reason for the divergence between the numerical and the experiment results at smaller values of δ/D may arise due to fact that shear modulus reduction of the soil with increasing strain amplitude was not considered in the soil model. Consequently, the peak bending strains within the pipe were overpredicted for smaller values of δ/D. All in all, Mohr-Coulomb model with use of the value of residual internal friction angle provides good estimations of pipe strains at large fault displacements while it may lead to conservative pipeline design under small fault displacements.

5. Calibration of the numerical model via a case history

The 1999 Kocaeli Earthquake (moment magnitude M_w of 7.6) hit Turkey on August 17, 1999 in its north-western part, see Fig. 17a for the location of the earthquake epicentre. The rupture length was approximately 150 km extending from the city of Duzce all the way to the Marmara Sea along the Izmit Gulf. The depth of hypocentre is approximately 15 km (Reilingeer et al., 2000). A butt-welded API Grade B steel

Thames water transmission pipeline crossing a strike-slip fault (Kullar Fault in Izmit, Turkey) failed due to large deformations imposed by the fault rupture as shown in Fig. 17b. The black dashed rectangular area on the map demonstrates the region where the Thames water pipeline crossed Kullar Fault. The detailed schematic sketch showing the Thames water transmission pipeline and fault location is shown in Fig. 18.

Eidinger et al. (2002) studied the performance of the Thames water transmission pipeline crossing Kullar fault. The diameter and wall thickness of the pipe were 2.2 m and 18 mm, respectively. The pipe-fault crossing angle (β) was 55.5° and maximum right-lateral offset of the fault was 3 m. The pipeline was subjected to bending and compressive strains due to the direction of the pipeline with respect to the fault trace. Two major local buckling (wrinkling) points were observed at both sides of the fault trace and one minor local buckling (wrinkling) also developed in the soft soil side as shown in Fig. 18. The effective internal diameter of the pipe was reduced at wrinkling points and this significantly influenced the performance of the pipeline in terms of flow rate. Partial tear and significant leak observed at wrinkle number 2 whereas
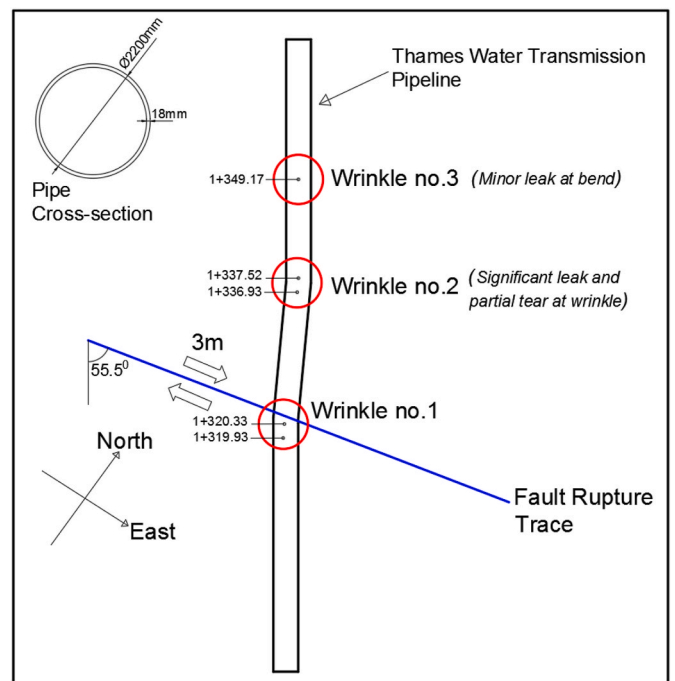

Fig. 18. The schematic illustration showing the locations of Thames water transmission pipeline with respect to fault rupture trace and wrinkling (local buckling) points on the pipeline (data used from Eidinger et al., 2002).

Fig. 17. a) A map of Turkey showing the epicentre of the 1999 Kocaeli Earthquake, b) a map showing the location of the Kullar Fault.

minor leak was observed at wrinkle number 3.

A quasi-static nonlinear analysis of the Thames water transmission pipeline crossing Kullar fault was performed using ABAQUS v 14 software. Three different loading stages were utilized to simulate real field conditions: (1) Gravity loading, (2) Internal pressure of the pipe, (3) Fault displacement. The gravity loading step was performed to simulate initial stresses in the soil and on the pipe due to the self-weight of the soil and pipe. In the second step, an internal pressure of 1 MPa was applied to the inner surface of the pipe to simulate operational stresses in the pipe. In the last step, a fault displacement of 3 m with a fault crossing angle 55.5° (1.70 m in the x-direction and 2.47 m in the y-direction) was applied to the right-hand side soil block and the left-hand side soil block was kept fixed. Equivalent boundary springs were connected at pipe ends to simulate axial continuity at pipe end boundaries. Solid continuum elements (C3D8R) were used to simulate soil and Mohr-Coulomb constitutive model was selected to represent the stress-strain relationship in the soil. Shell elements (S4R) were used to simulate the pipeline. Isotropic Von Mises yield model was chosen to represent stress-strain behaviour of the pipe material. Tangential and normal contacts were used to simulate interactions at soil-pipe interface. The friction coefficient (μ_f) between the soil and pipe surfaces was taken as 0.3. The vertical boundary nodes of the fixed parts were restricted in the horizontal direction. The fault characteristics, pipe and soil parameters used in the numerical analysis are given in Table 8.

The side and plan view of the 3D FE model showing equivalent boundary springs at pipe ends, dimensions of 3D FE model and soil movement due to fault displacement along with the legend of displacements are shown in Fig. 19. The displacement values (U) in the legend are in meters. Fig. 20 shows Mises stresses within the pipeline and as well as a minor wrinkling point (Wrinkling No.3) and two major wrinkling points (Wrinkling No.1 and No.2) occurring due to the fault movement. The units of the Mises stresses in the pipeline is in Pascal (Pa) as seen in the legend. Since soil properties are different at both sides of the fault line (one side is stiff soil, other is soft soil) an asymmetric pipe deflection about the fault trace is observed as seen in Fig. 20. It is obvious that the location of Wrinkling No.1 (in stiff soil) is closer to the fault trace than the location of Wrinkling No.2 (in soft soil) is. The plastic longitudinal pipe strains (PE) along the pipeline are shown in Fig. 21a and the plastic longitudinal pipe strains at the wrinkling points are focused on in Fig. 21b.

The observed and calculated plastic deformations of the Thames water transmission pipe due to the fault movement in the 1999 Kocaeli Earthquake are shown in Fig. 22a–b. The photo of the deformed Thames water pipe is taken from the work of Kaya et al. (2017). The calculated and observed plastic deformation patterns looks quite similar as seen in Fig. 22a–b. Table 9 highlights key results observed from the case study of the Thames water pipeline crossing Kullar fault and obtained from 3D FE analysis. The separation distance between Wrinkling No.1 and

Wrinkling No.2 (major wrinkles) was observed as 14 m from the numerical analysis (see Fig. 20) while this distance was specified around 17.1 m–17.6 m from field observations. This difference between calculated and observed separation distance may be due to that the soil model used in the numerical analysis showed stiffer response compared to the soil response in real field. Pipe strains are localized over shorter pipe length when soil surrounding the pipeline gets stiffer so that separation distance between Wrinkling No.1 and Wrinkling No.2 calculated by the numerical analysis is smaller relative to that observed in the field. The rotation demands of pipe wrinkles were obtained as 8.5–10° from the numerical analysis while those values obtained from the field observation were 7.5–8.5°. The distance between Wrinkling No.3 and Wrinkling No.2 was obtained as 12.0 m from the numerical analysis whereas this distance was observed as 13.0 m in the field. The comparison shows that the results obtained by numerical analysis and field observations are quite consistent considering rotation demands of pipe wrinkles and separation distance between Wrinkling No.3 and Wrinkling No.2.

6. A parametric study on buried continuous steel pipelines crossing strike-slip faults

The validated three-dimensional (3D) Finite Element (FE) models were used to conduct a parametric study to investigate the effects of governing non-dimensional groups on the behaviour of buried continuous steel pipelines. Totally eighty-four FE analysis were performed in the scope of the parametric study. The plan of numerical study is shown in Table 10, in detail. The schematic sketch showing Case 1 and Case 2 is illustrated in Fig. 23. The parameters used in the numerical study are summarised in Table 11. Numerical results were obtained for the steel pipeline with 0.9144 m diameter for various slenderness ratio (D/t) and for different soil conditions. Three values of the pipe wall thickness (t) were used such as 7.62 mm, 11.91 mm, and 15.24 mm, corresponding to D/t values equal to 120, 76.78 and 60, respectively. These values of the ratios of the pipe diameter to wall thickness (D/t) are commonly used in oil and gas pipeline networks, as well as water transmission pipelines (Vazouras et al., 2010). API 5 L X70 steel pipe with 490 MPa of yield strength was used in the parametric study. The Young's Modulus of the steel pipe was taken as 210 GPa in the numerical analysis. Two different operation pressure of the pipeline were selected: (a) no pipe pressure is considered ($p/\sigma_y = 0$), and (b) pipe operation pressure is equal to 6.29 MPa corresponding to the value of $p/\sigma_y = 0.0134$. The pipeline was assumed to be placed in the clay soil with different cohesion values at 2.5 m burial depth so that wide range of relative soil-pipe stiffness values was covered. The values of kD^4/EI range from 0.0007 to 0.0217, see Table 11. The term k is the lateral soil spring stiffness and it was calculated by using the equations proposed in ALA Guidelines (2005).

The dimensions of the model for Case 1 were 20 m in x direction, 5 m in y direction and 60 m in z direction as seen in Fig. 24. Three different loading stages were utilized to simulate the pipeline crossing strike-slip faults: (1) Gravity loading was applied to the whole model, (2) pipe pressure was applied to the inner surface of the pipeline and (3) the fault displacement was applied to movable soil block with a fault crossing angle of −20° (the pipeline is under tension and bending) and fixed soil block was restrained in horizontal and axial directions (see Fig. 23).

Fig. 25 shows the 3D FE model for Case 2 along with the cross-section view of the soil block, the plan view of the deflected soil blocks and the plan view of the deflected pipeline. The dimensions of 3D FE model are shown in Fig. 25. Three different loading stages were used to simulate the soil-pipe interaction problem under strike-slip faulting as in Case 1: (1) gravity loading, (2) internal pipe pressure and (3) fault displacement. The fault displacement was applied to the movable block with a fault crossing angle of +20° (the pipeline is under compression and bending) and fixed soil block was restrained in horizontal and axial directions as shown in Fig. 25.

Fig. 26 plots the longitudinal pipe strain distribution at a spring-line

Table 8
Fault Characteristics, soil and pipe properties (Eidinger et al., 2002; Kaya et al., 2017).

| Pipe and Fault Characteristics		Soil Parameters	
Pipe Material	API Grade B Steel	Soft Soil	
Pipe Diameter, D (m)	2.2	Young's Modulus (MPa)	8
Pipe Wall Thickness, t (m)	0.018	Cohesion (kPa)	20
Slenderness Ratio (D/t)	125		
Pipe Burial Depth (m)	3.05	Stiff Soil	
Fault crossing angle, β	55.5°	Young's Modulus (MPa)	16
Fault Offset, δ (m)	3	Cohesion (kPa)	40
Transverse Offset (m) (y-direction)	2.47		
Longitudinal Offset (m) (x-direction)	1.7		
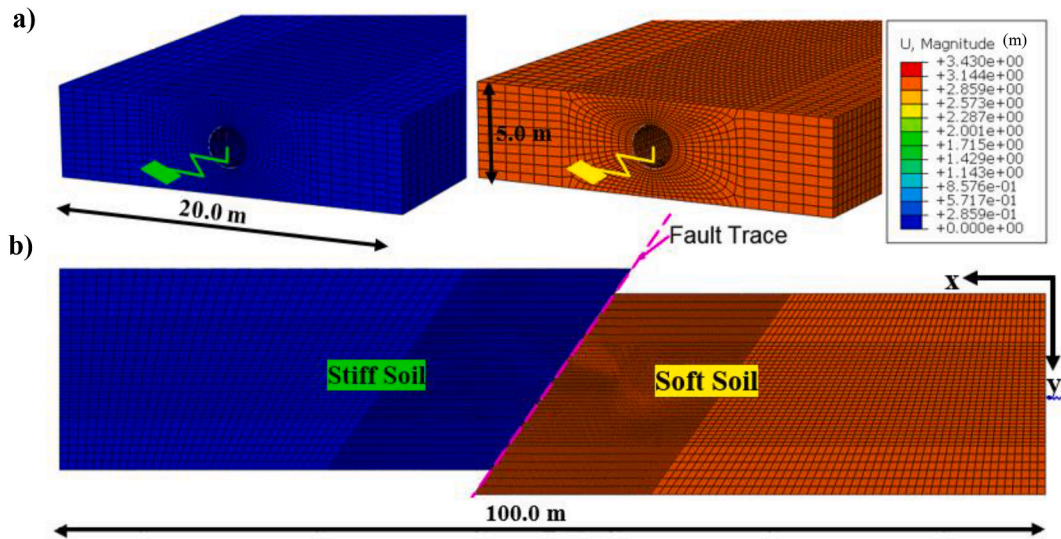
Fig. 19. a) Side view of the three-dimensional (3D) Finite Element (FE) model showing cross-section dimensions and equivalent end boundary springs, b) plan view of the 3D FE model showing length of the model and soil movement due to the fault displacement.
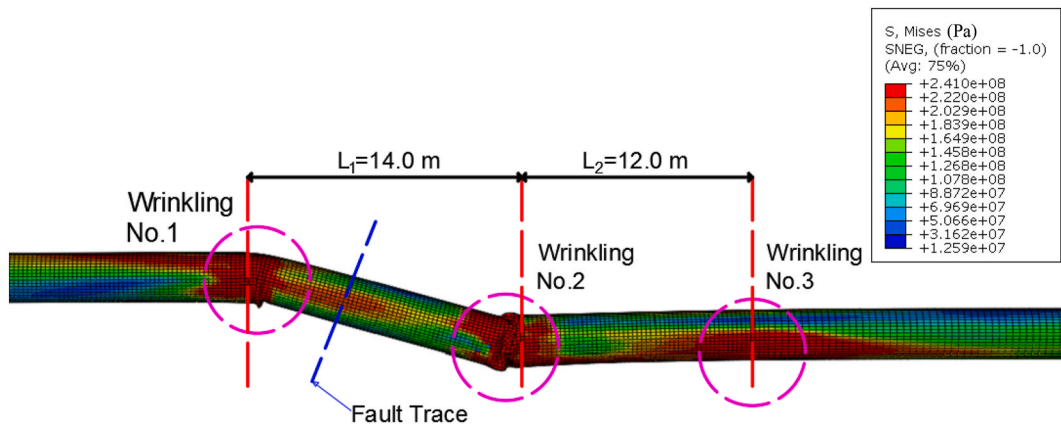

Fig. 20. The Mises stresses along the pipeline developing due to gravity, inner pipe pressure and fault displacement loading.
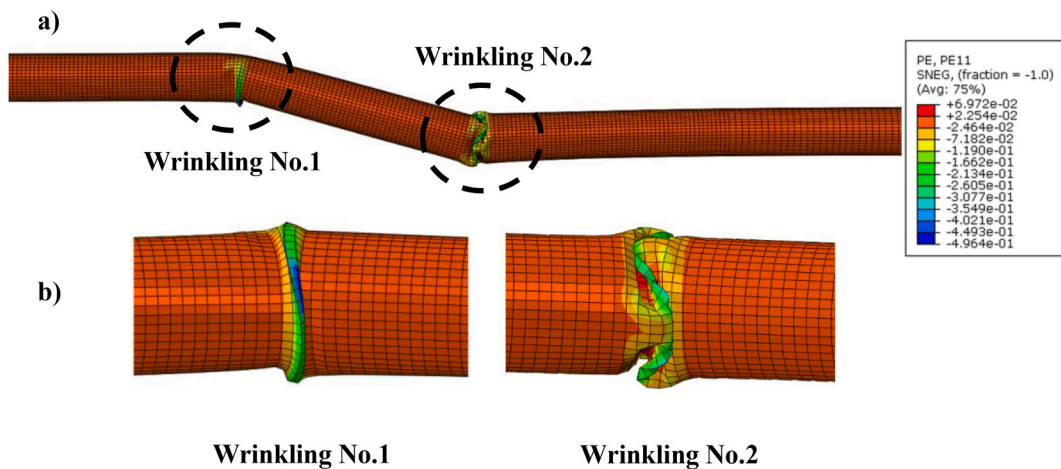

Fig. 21. a) The plastic longitudinal pipe strains (PE) along the pipeline, b) PE at the wrinkling points.

for Case 1 under varying fault displacements. The normalized fault displacements (δ/D) range between 0.19 and 1.04. The ratio of the pipe diameter to wall thickness (D/t), the ratio of burial depth to pipe diameter (H/D), normalized pipe pressure (p/σ_y) and relative soil-pipe stiffness is equal to 76.78, 2.73, 0 and 0.0047, respectively. As seen in the figure, longitudinal strain distribution shows symmetrical behaviour at around fault trace under small fault displacements (e.g. $\delta/D = 0.19$) whereas tensile strains localize at around $5.5 \times D$ (5.5 pipe diameter)

Fig. 22. a) Observed plastic deformations of the Thames water transmission pipe aftermath of the 1999 Kocaeli Earthquake (Kaya et al., 2017), b) calculated plastic deformations of the Thames water transmission pipeline.

Table 9
Comparison of the field measurements and numerical results.

	The separation distance between wrinkles 1 and 2 (m)	Rotations at Wrinkles (1 and 2)	The distance between 2nd and 3rd wrinkle (m)
Field Observations[a]	17.1–17.6	7.5–8.5°	13.0
3D FEA	14	8.5–10°	12.0

[a] The data for the field observations is taken from the work of Kaya et al. (2017).

Table 10
The plan of the parametric study.

Case 1	$p/\sigma_y = 0$	21 models[a]
Case 1	$p/\sigma_y = 0.0134$	21 models[a]
Case 2	$p/\sigma_y = 0$	21 models[a]
Case 2	$p/\sigma_y = 0.0134$	21 models[a]

[a] 21 various values of KD^4/EI, see Table 11.

distance from the fault trace under larger fault displacements (e.g. $\delta/D = 1.04$).

Longitudinal pipe strain distributions at a spring-line for Case 2 under various fault displacements are plotted in Fig. 27. The normalized fault displacements (δ/D) range between 0.19 and 1.04. The ratio of the pipe diameter to wall thickness (D/t), the ratio of burial depth to pipe diameter (H/D), normalized pipe pressure (p/σ_y) and relative soil-pipe stiffness (kD^4/EI) is equal to 76.78, 2.73, 0 and 0.0047, respectively. Longitudinal strain distribution shows symmetrical behaviour at around fault trace under small fault displacements (e.g. $\delta/D = 0.19$) whereas compressive strains localize at around $4.4 \, x \, D$ (4.4 pipe diameter) distance from the fault trace under larger fault displacements (e.g. $\delta/D = 1.04$).

Fig. 28 demonstrates the variation of maximum tensile strain ($\varepsilon_{T,max}$) with respect to normalized fault displacements (δ/D) for various relative soil-pipe stiffness (kD^4/EI). The results demonstrated in the figure is for the steel pipeline with $p/\sigma_y = 0$ and $D/t = 76.78$ for Case 1. $\varepsilon_{T,max}$ developing within the pipeline increase with the increase in δ/D and kD^4/EI. Three different zones can clearly be observed: a) in the first zone where is between 0 and 0.25D fault displacements, the values of
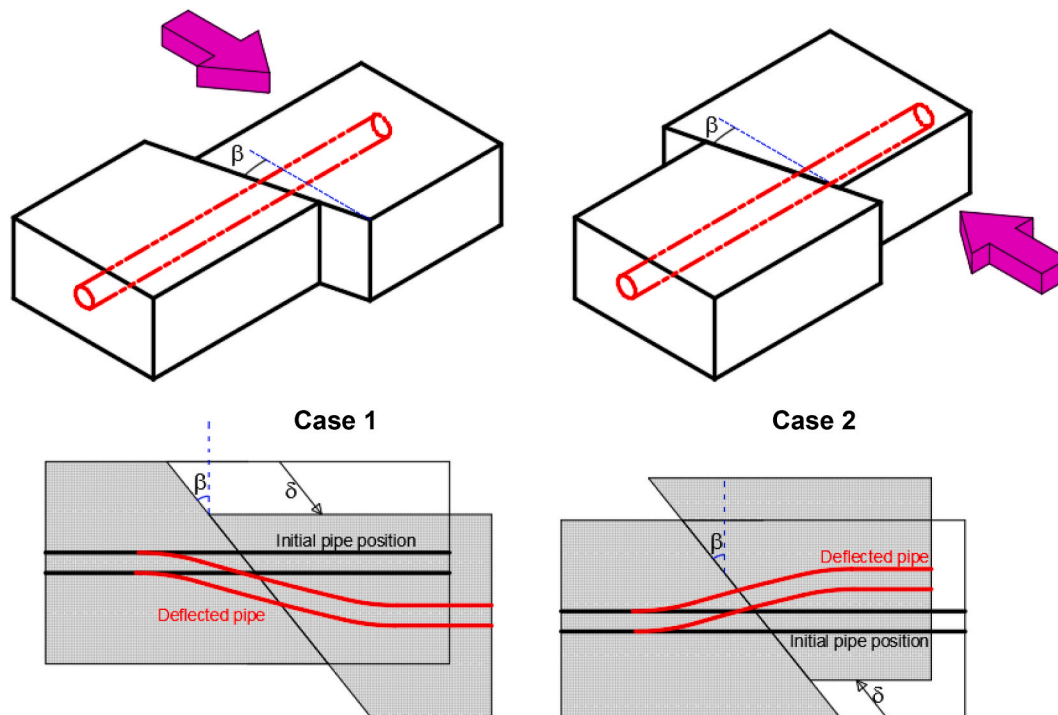

Fig. 23. a) Case 1: Pipelines crossing strike-slip faults with $\beta = 20°$ (pipelines are under tension and bending), b) Case 2: Pipelines crossing strike-slip faults with $\beta = 20°$ (pipelines are under compression and bending).

Table 11
Input parameters used in 3D FE analysis.

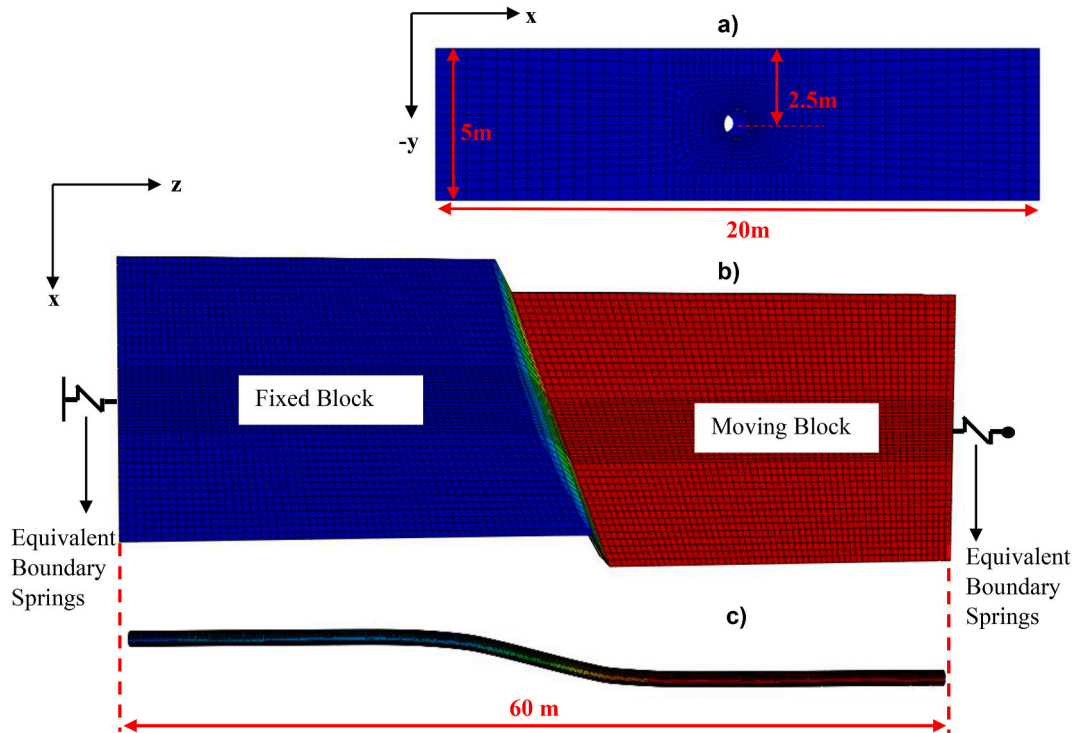| Pipe Diameter (D)	Pipe Wall Thickness (t)	Pipe Pressure (p)	Pipe yield stress (σ_y)	Clay Cohesion (c)	Relative Soil-Pipe Stiffness (kD^4/EI)	Pipe Slenderness Ratio (D/t)	Normalized Pipe Pressure (p/σ_y)
m	*m*	*MPa*	*MPa*	*kPa*	–	-	–
0.9144	0.00762	0 and 6.59	490	10	0.0014	120	0 and 0.0134
				30	0.0043		
				50	0.0072		
				70	0.0101		
				90	0.0130		
				125	0.0181		
				150	0.0217		
0.9144	0.01191	0 and 6.59		10	0.0009	76.78	
				30	0.0028		
				50	0.0047		
				70	0.0066		
				90	0.0085		
				125	0.0118		
				150	0.0141		
0.9144	0.01524	0 and 6.59		10	0.0007	60	
				30	0.0022		
				50	0.0037		
				70	0.0052		
				90	0.0067		
				125	0.0093		
				150	0.0112		

Fig. 24. 3D FE model of Case 1: a) Cross-section of soil prism showing cross-section dimensions of the soil blocks, b) plan view of the deflected soil blocks, c) plan view of deflected pipeline showing the length of the model.

maximum tensile strains linearly increase, b) in the second zone where is between $0.25D$ and $2.75D$ to $3.25D$, there is a decreasingly growing nonlinear relation between $\varepsilon_{T,max}$ and δ/D for all kD^4/EI values, c) in the third zone where starts after $2.75D$ to $3.25D$, there is an increasingly growing relation between $\varepsilon_{T,max}$ and δ/D for all values of kD^4/EI. Purple dashed circles placed on the figure show the points where necking type of pipe failure initiates for various values of relative soil-pipe stiffness. The necking failure develops at smaller fault displacements as the value of relative soil-pipe stiffness increases.

Fig. 29 shows the variation of maximum compressive strain ($\varepsilon_{C,max}$) with increasing normalized fault displacements (δ/D) for different

values of relative soil-pipe stiffness (kD^4/EI). The results demonstrated in the figure is for the steel pipeline with $p/\sigma_y = 0$ and $D/t = 76.78$ for Case 2. $\varepsilon_{C,max}$ developing within the pipeline increase with the increase in δ/D and kD^4/EI. As seen in the figure, the pipeline experiences local buckling even for very small values of fault displacements ($0 - 0.5D$) for all values of kD^4/EI. After initiation of the local buckling within the pipe wall, strain localization develops and maximum compressive pipe strains ($\varepsilon_{C,max}$) increasingly grows.

Figs. 28 and 29 show typical results for variation of maximum tensile and compressive strains with increasing normalized fault displacements.
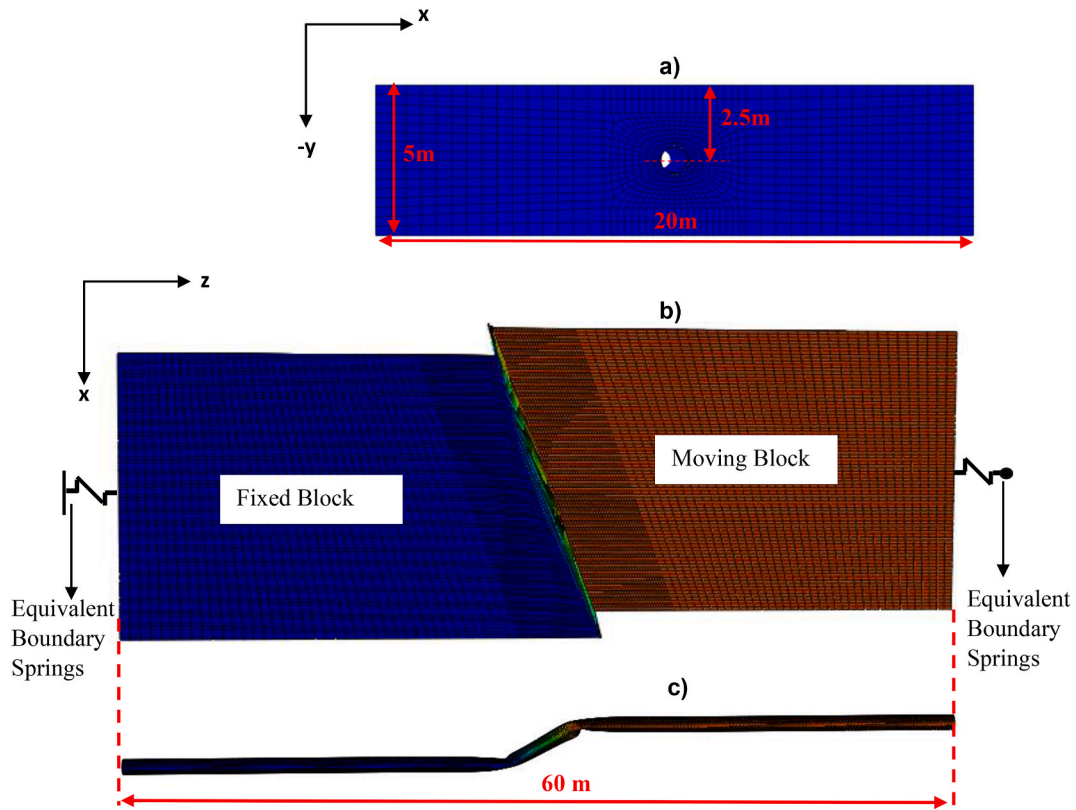
Fig. 25. 3D FE model of Case 2: a) Cross-section of soil prism showing cross-section dimensions of the soil blocks, b) plan view of the deflected soil blocks, c) plan view of deflected pipeline showing the length of the model.
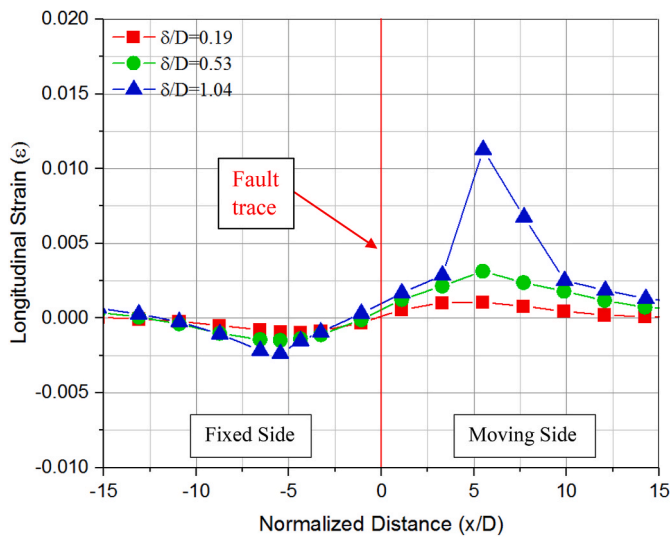

Fig. 26. Longitudinal pipe strain at a spring-line for Case 1 under various fault displacements (p = 0, D/t = 76.78, H/D = 2.73, kD^4/EI = 0.0047).

Fig. 27. Longitudinal pipe strain at a spring-line for Case 2 under various fault displacements (p/σ_y = 0, D/t = 76.78, H/D = 2.73, kD^4/EI = 0.0047).

These results are for the pipelines with $D/t = 76.78$, $H/D = 2.73$, $p/\sigma_y = 0$. The same results (maximum tensile and compressive strain vs. normalized fault displacements) can be plotted for the pipelines having other values of D/t, H/D and p/σ_y. Using these plots and considering performance limit criteria such as tensile failure and local buckling, the graphs for estimating critical fault displacements were proposed as seen in Figs. 30 and 31.

Fig. 30a–c demonstrates the variation of critical normalized fault displacements $((\delta/D)_{cr})$ with respect to relative soil-pipe stiffness for
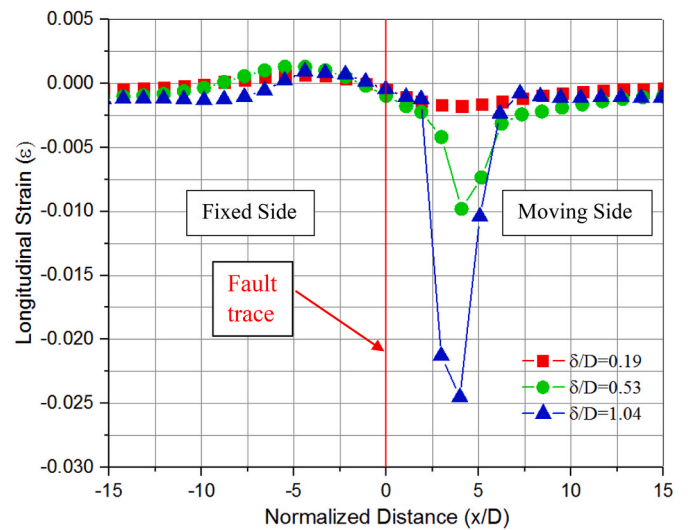
various ratios of D/t, p/σ_y and H/D. The values of $(\delta/D)_{cr}$ are obtained for 2% tensile failure criteria for various values of kD^4/EI, D/t, H/D and p/σ_y These data points demonstrate the values of $(\delta/D)_{cr}$, where the maximum tensile strain reaches at 2% of tensile strain, for different ratios of D/t, H/D and p/σ_y. As seen in Fig. 30a–c, the values of $(\delta/D)_{cr}$ logarithmically decrease with the increase in kD^4/EI. The performance of buried continuous pipelines under tension and bending can be improved by decreasing the D/t ratio of pipelines as seen in Fig. 30a. The performance increase with decreasing the D/t ratio becomes less
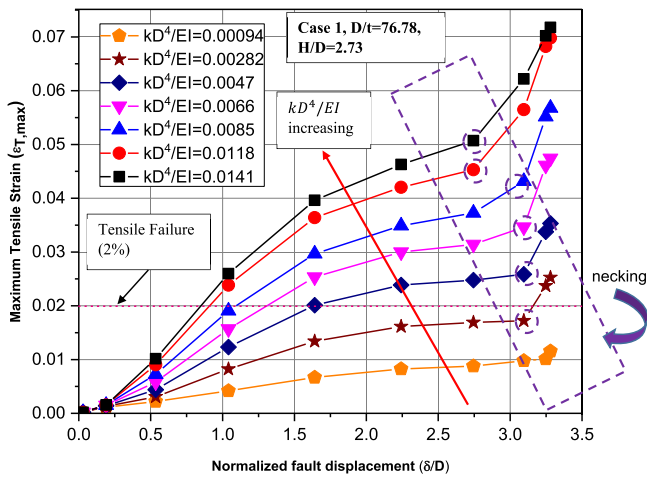
Fig. 28. Variation of maximum tensile strain ($\varepsilon_{T, max}$) with respect to normalized fault displacements (δ/D) for various relative soil-pipe stiffness (kD^4/EI) (Case 1, $p/\sigma_y = 0$, D/t = 76.78, H/D = 2.73).
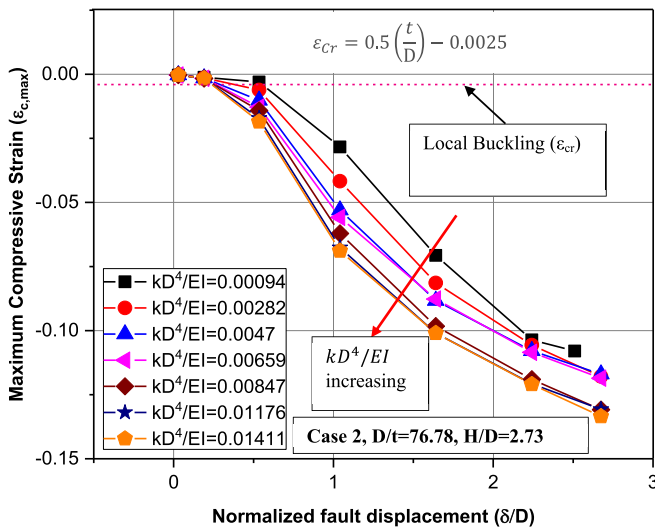

Fig. 29. Variation of maximum compressive strain ($\varepsilon_{C, max}$) with respect to normalized fault displacements (δ/D) for various relative soil-pipe stiffness (kD^4/EI) (Case 2, $p/\sigma_y = 0$, D/t = 76.78, H/D = 2.73).

significant with increasing pipe flexibility. For instance, the performance of the pipeline in terms of $(\delta/D)_{cr}$ increased by 150% (from 1.3 to 3.25) at $kD^4/EI = 0.004$ by decreasing the D/t ratio from 120 to 60 while the performance increase is 47% at $kD^4/EI = 0.011$ by changing the D/t ratio from 120 to 60. Fig. 30b plots the variation of $(\delta/D)_{cr}$ with increasing pipe flexibility for various p/σ_y ratios. As seen in the figure, the increase in pipe internal pressure slightly decreases pipeline performance under faulting. Fig. 30c plots the variation of $(\delta/D)_{cr}$ with increasing pipe flexibility for various H/D ratios. Decreasing the ratio of H/D increases pipeline performance in terms of $(\delta/D)_{cr}$ as seen in the figure.

Fig. 31a–c shows the variation of the $(\delta/D)_{cr}$ with the change in kD^4/EI, H/D, D/t and p/σ_y for local buckling failure criteria. The data points demonstrate the values of $(\delta/D)_{cr}$, where the maximum compressive strain reaches at local buckling failure strain, for different values of kD^4/EI, D/t, H/D and p/σ_y. Decreasing the ratio of D/t increases pipeline performance as seen in Fig. 31a. However, the performance increase with decreasing the D/t ratio becomes less significant with increasing pipe flexibility. For instance, the performance of the pipeline in terms of
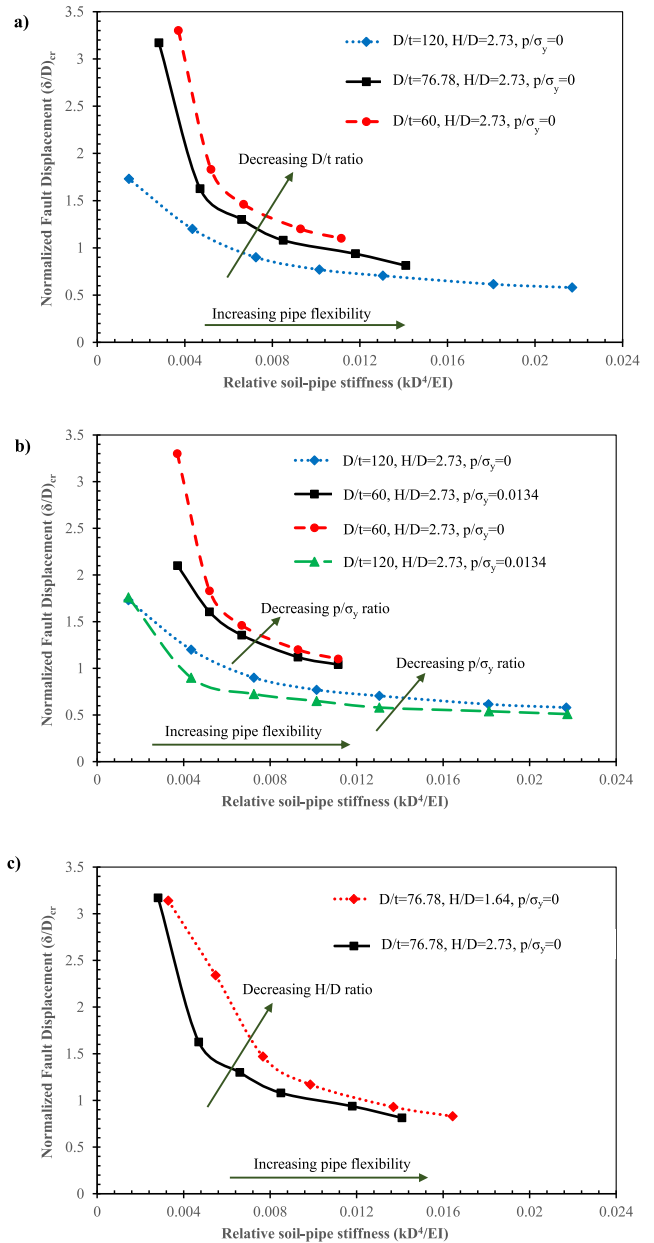

Fig. 30. Tensile Failure Case (Case 1): Variation of critical normalized fault displacements (δ/D)$_{cr}$ with respect to various relative soil-pipe stiffness (kD^4/EI), a) for various D/t ratios, b) for various p/σ_y ratios and c) for various H/D ratios.

$(\delta/D)_{cr}$ increased by 280% (from 0.2 to 0.76) at $kD^4/EI = 0.0016$ by decreasing the D/t ratio from 120 to 60 while the performance increase is 122% at $kD^4/EI = 0.011$ by changing the D/t ratio from 120 to 60. Fig. 31b plots the variation of $(\delta/D)_{cr}$ with increasing pipe flexibility for various p/σ_y ratios. As seen in the figure, thicker pipelines ($D/t = 60$) are slightly influenced by increasing pipe internal pressure (p/σ_y) compared to thinner pipelines ($D/t = 120$). The performance decrease in terms of $(\delta/D)_{cr}$ is very small with the increase in (p/σ_y) for both thicker and thinner pipelines. Decreasing H/D ratio increases the performance of pipelines in the range of $kD^4/EI = 0 - 0.01$. However, the performance increase with decreasing the pipe burial depth is negligible beyond the value of $kD^4/EI = 0.01$.
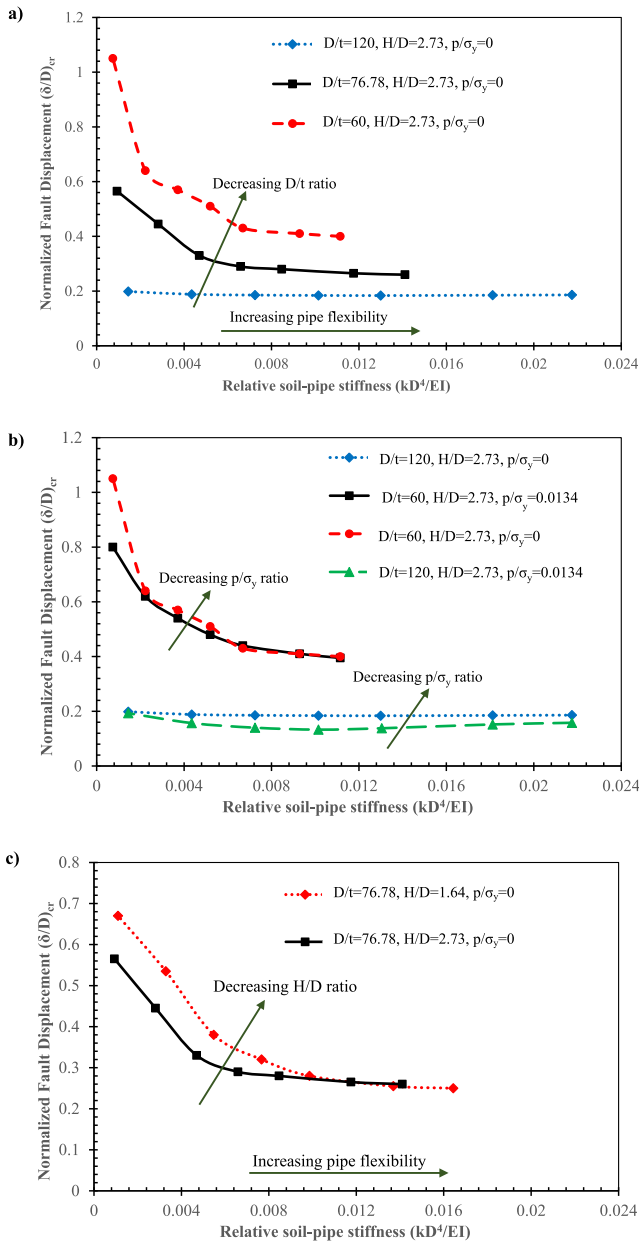
Fig. 31. Local Buckling Case (Case 2): Variation of critical normalized fault displacements (δ/D)$_{cr}$ with respect to various relative soil-pipe stiffness (kD^4/EI), a) for various D/t ratios, b) for various p/σ_y ratios and c) for various H/D ratios.

7. The effect of pipe end conditions on buried continuous pipelines crossing strike-slip faults

Six different three-dimensional (3D) Finite Element (FE) analysis were performed to investigate the effects of pipe end boundary conditions on buried continuous pipeline response to strike-slip faulting. Three various pipe end boundary conditions for Case 1 and Case 2 were considered: (a) fixed-fixed end conditions (Fig. 32a), (b) equivalent boundary spring-equivalent boundary spring end conditions (Fig. 32b), and (c) free-free end conditions (Fig. 32c).

For the fixed-fixed pipe end conditions, the fault displacement was applied at the pipe end on the moving side: The blue arrow shows the direction of the applied fault movement for Case 1 (the pipeline is under bending and tension) while the red arrow shows the direction of applied fault movement for Case 2 (the pipeline is under bending and

compression) as seen in Fig. 32a. In addition, the pipe end was fixed on the stationary side. For the equivalent boundary spring-equivalent boundary spring end conditions, the fault displacement was applied at the spring end on the moving side: Red arrow shows the direction of applied fault movement for Case II while blue arrow shows the direction of the applied fault movement for Case 1 as seen in Fig. 32b. In addition, the end of equivalent boundary spring on the stationary side is fixed. For the third scenario (free-free end conditions), the pipe ends at both stationary and moving side were kept free as seen in Fig. 32c.

The same 3D FE numerical models that were explained in Section 6 were used for the parametric study. A steel pipeline with 914.4 mm diameter and 11.91 mm wall thickness was used in the numerical models. The pipeline was assumed to be buried in a clay soil with a cohesion of 50 kPa at a burial depth of 1.5 m. The pipe material was modelled by using a Young's modulus of 210 GPa and a yield strength of 490 MPa. The parameters used in the numerical analysis are summarised in Table 12. Fig. 33 plots variation of maximum tensile strains with increasing normalized fault displacements for Case 1. The double purple circles show the points where necking failure starts to develop. For the case of fixed-fixed end condition, the buried continuous pipeline experiences a necking form of failure at even small normalized fault displacements (at around $\delta = 0.5D$). The maximum tensile strain within the pipeline shows exponential growth with increasing normalized fault displacements. For the case of equivalent boundary spring-equivalent boundary spring end condition, the necking form of failure starts to develop at relatively larger normalized fault displacement ($\delta = 3.10D$) compared to the fixed-fixed end condition. In contrast to the fixed-fixed end condition, the maximum tensile strain experiences logarithmic growth with increasing normal fault displacements until the necking of the pipeline develops. After initiation of the necking form of failure, the maximum tensile strain increases exponentially with under increasing normalized fault displacements. For the case of free-free end conditions, maximum tensile strain within the pipeline experiences logarithmic growth and necking type of failure was not observed in the interval of $\delta = 0D$ and $\delta = 3.5D$.

Fig. 34 plots variation of maximum compressive strains with increasing normalized fault displacements for Case 2: buried continuous pipelines under bending and compression for various pipe end conditions. The double purple circles show the points where local buckling failure starts to develop. Local buckling failure starts to develop at very small normalized fault displacement ($\delta = 0.25D$) for the case of fixed-fixed end condition. The buried continuous pipeline experiences local buckling failure at around $\delta = 0.5D$ for the case of end boundary spring-end boundary spring end condition while local buckling failure develops at around $\delta = 1.0D$ for the case of free-free end conditions. A logarithmic growth trend in the maximum compressive strain has been observed for all the cases.

8. Discussions and conclusions

A newly developed physical model test setup of buried pipelines crossing strike-slip faults is described in detail along with the derivation of relevant scaling laws and similitude relations. The physical meaning of governing non-dimensional groups and the values of their practical range are presented. The results of experiments in terms of bending and axial strains are also presented. A three-dimensional (3D) Finite Element model is developed and calibrated through the model test results and the validated model is used to simulate a field case record. The validated numerical model was also used to perform a parametric study for investigating the parameters influencing the pipeline response to strike-slip faulting and studying the effects of pipe end conditions on the behaviour of buried continuous pipelines crossing strike-slip faults.

The main conclusions of the study are as follows:

1) Peak axial and bending strains increase with the increase in the H/D ratio i.e. for deeper burial depths. It is therefore concluded that
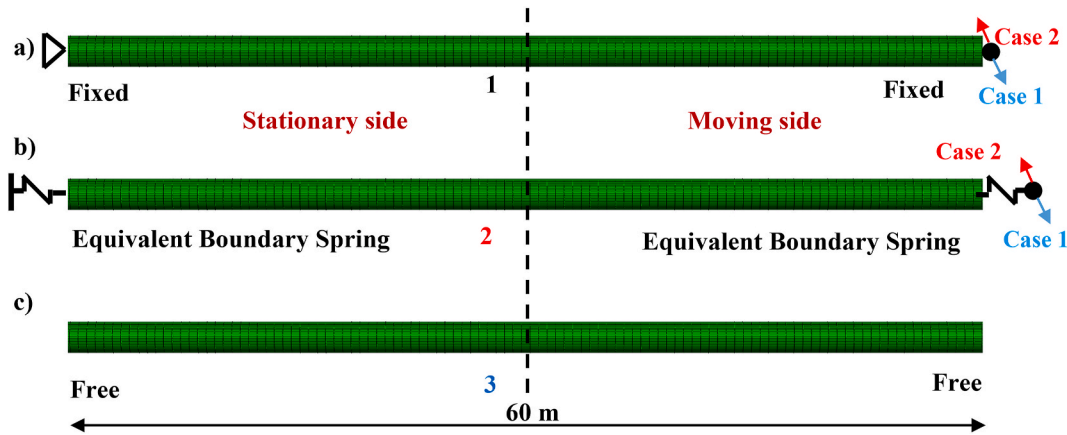
Fig. 32. Pipe end boundary conditions: a) fixed-fixed end conditions, b) equivalent boundary spring-equivalent boundary spring end conditions, c) free-free end conditions.

Table 12
The parameters used in the numerical analysis.

Soil		Pipe	
E (MPa)	20	E (GPa)	210
ν	0.35	ν	0.3
c (kPa)	50	σ_y (GPa)	0.49
Geometry			
D (m)	0.9144	D/t	76.78
t (m)	0.01191	H/D	1.64
H (m)	1.5		

Fig. 34. Case 2: Maximum compressive strain ($\varepsilon_{C,\,max}$) vs. normalized fault displacement (δ/D).
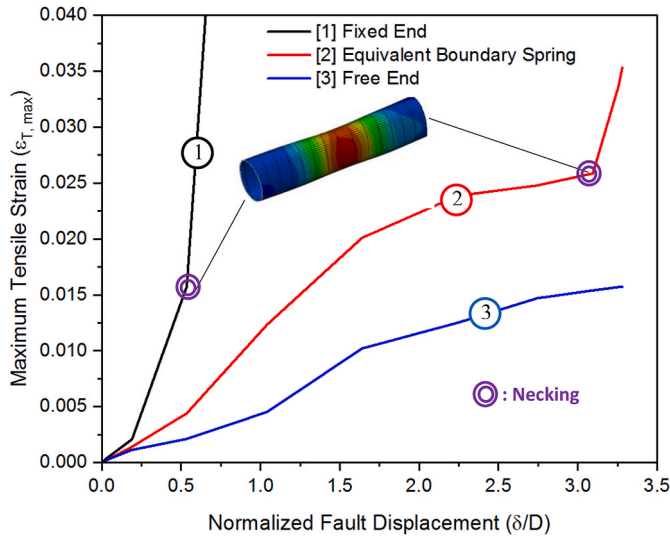

Fig. 33. Case 1: Maximum tensile strain ($\varepsilon_{T,\,max}$) vs. normalized fault displacement (δ/D).

pipelines crossing active faults should be buried at shallow depths in order to reduce axial and bending strains developing within pipelines.

2) Buried pipelines crossing strike-slip faults with a fault crossing angle of $\beta = 90°$ experience much smaller peak axial strains compared to those crossing strike-slip faults with a fault crossing angle of $\beta < 90°$. Therefore, buried pipelines crossing faults with an angle of 90° is considered as the most preferable case.

3) Buried pipelines subjected to compression and bending due to faulting experience much larger bending and axial strains compared to those subjected to tension and bending due to the occurrence of local buckling. Therefore, it is concluded that the route of buried
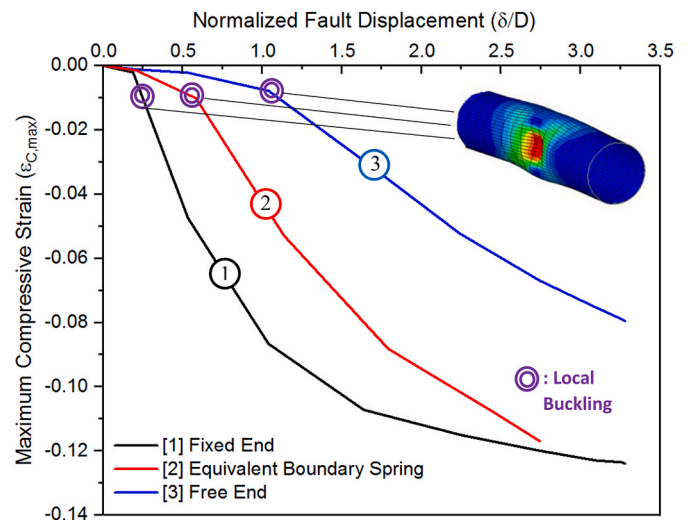
pipelines should be chosen in such a way that they are subjected to tension and bending forces rather than compression and bending.

4) Decreasing the D/t ratio of pipelines increases the pipeline performance at fault crossings. Consequently, thicker pipelines (with smaller D/t ratios) are suggested to be used at fault crossings.

5) The increase in relative soil-pipe stiffness (kD^4/EI) increases peak bending and axial strains. Therefore, pipelines should be buried at shallow depths and in soft soils such as loose sands or soft clays at fault crossings to reduce peak bending and axial strains.

6) The increase in normalized pipe internal pressure (p/σ_y) decreases the pipeline performance under strike-slip faulting in terms of critical normalized fault displacements. Thicker pipelines are slightly influenced by the increase in pipe internal pressure compared to thinner pipelines. Therefore, thicker pipelines should be selected for cases of high-pressure pipelines crossing active faults.

7) Buried continuous pipelines experience necking or local buckling form of failure at even small normalized fault displacements when pipe ends are fixed. Therefore, axial/bending constraints such as anchor/thrust blocks, pump station or bents should be avoided at the vicinity of fault crossings to minimise longitudinal pipe strains and to increase the performance of buried continuous pipelines crossing active faults.

Credit author statement

Hasan Emre Demirci: Conceptualization, Methodology, Experiments, Numerical Models, Writing – original draft preparation, Mustafa Karaman: Experiments, Subhamoy Bhattacharya: Reviewing and Editing, Supervision

Declaration of competing interest

The authors declare that they have no known competing financial interests or personal relationships that could have appeared to influence the work reported in this paper.

Acknowledgements

References

Abaqus Analysis User's Analysis Manual, 2014. Dassault Systèmes Simulia Corp., Providence, RI, USA.

Abdoun, T.H., Ha, D., O'Rourke, M.J., Symans, M.D., O'Rourke, T.D., Palmer, M.C., Stewart, H.E., 2009. Factors influencing the modelling of buried pipelines subjected to earthquake faulting. Soil Dynam. Earthq. Eng. 29, 415–427.

ALA (American Lifelines Alliance), 2005. Seismic Guidelines for Water Pipelines. FEMA, Washington, DC.

ASCE, 1984. Guidelines for the Seismic Design of Oil and Gas Pipeline Systems, Committee on Gas and Liquid Fuel Lifelines, American Society of Civil Engineers, Reston, VA.

American Society of Mechanical Engineers, 2006. Pipeline transportation systems for liquid hydrocarbons and other liquids. ANSI/ASME B31, 4.

American Society of Mechanical Engineers, 2007. Gas transmission and distribution piping systems. ANSI/ASME B31, 8.

Banushi, G., Squeglia, N., Thiele, K., 2018. Innovative analysis of a buried operating pipeline subjected to strike-slip fault movement. Soil dyn. Earthquake Eng. 107, 234–249.

Bhattacharya, S., Demirci, H.E., Nikitas, G., Prakhya, G.K.V., Lombardi, D., Alexander, N. A., Aleem, M., Amani, S., Mylonakis, G., 2021. Physical Modeling of Interaction Problems in Geotechnical Engineering. Modeling in Geotechnical Engineering. Academic Press, pp. 205–256. https://doi.org/10.1016/B978-0-12-821205-9.00017-4. ISBN 9780128212059.

Bolton, M.D., 1986. The strength and dilatancy of sands. Geotechnique 36 (1), 65–78.

Bolton, M.D., Gui, M.W., Phillips, R., 1993. Review of miniature soil probes for model tests. In: Proceedings of 11th South East Asia Geotechnical Conference, pp. 85–91 (Singapore).

Buckingham, E., 1914. The interpretation of experiments on models,. J. Wash. Acad. Sci. 93, 336.

Demirci, H.E., Bhattacharya, S., Karamitros, D.K., Alexander, N., 2018. Experimental and numerical modelling of buried pipelines crossing reverse faults. Soil Dynam. Earthq. Eng. 114, 198–214.

Demirci, H.E., 2019. Experimental and Numerical Modelling of Buried Continuous Pipelines Crossing Active Faults. Doctoral thesis. University of Surrey.

Dickin, E.A., Leuoy, C.F., 1983. Centrifuge model tests on vertical anchor plates. ASCE J Geotechnical Engineering 109 (12), 1503–1525.

EERI, 2008. The Wenchuan, Sichuan Province, China, Earthquake of May 12, 2008. Report, October 2008. EERI Special Earthquake.

EEFIT, 2009. The L'aquila, Italy Earthquake of 6 April 2009. A Preliminary Field Report by EEFIT.

EERI, 2010. The Mw 8.8 Chile Earthquake of February 27, 2010. Report, June 2010. EERI Special Earthquake.

Eidinger, J.M., O'Rourke, M., Bachhuber, J., 2002. Performance of a pipeline at a fault crossing. In: 7th U.S. National Conference of Earthquake Engineering. July21– 25. Earthquake Engineering Research Institute (EERI), Boston.

Ha, D., Abdoun, T.H., O'Rourke, M.J., Symans, M.D., O'Rourke, T.D., Palmer, M.C., Stewart, H.E., 2008. Buried high-density polyethylene pipelines subjected to normal and strike-slip faulting – a centrifuge investigation. Can. Geotech. J. 45, 1733–1742.

Ha, D., Abdoun, T.H., O'Rourke, M.J., Symans, M.D., O'Rourke, T.D., Palmer, M.C., Stewart, H.E., 2010. Earthquake faulting effects on buried pipelines-case history and centrifuge study. J. Earthq. Eng. 14 (5), 646–669.

International Technical Committee Tc2, 2005. Catalogue of Scaling Laws and Similitude Questions in Centrifuge Modelling.

Kaya, E.S., Uckan, E., O'Rourke, M.J., Karamanos, S.A., Akbas, B., Cakir, F., Cheng, Y., 2017. Failure analysis of a welded steel pipe at Kullar fault crossing. Eng. Fail. Anal. 71, 43–62.

Kennedy, R.P., Chow, A.W., Williamson, R.A., 1977. Fault movement effects on buried oil pipeline. Transportation Engineering Journal. ASCE 103 (5), 617–633.

Liu, A.W., Hu, Y.X., Zhao, F.X., Li, X.J., Takada, S., Zhao, L., 2004. An equivalent boundary method for the shell analysis of buried pipelines under fault movement. ACTA Seismol Sin 2004 17 (Suppl. 1), 150–156. https://doi.org/10.1007/s11589-004-0078-1 [2004].

Liu, X., Zhang, H., Li, M., Xia, M., Zheng, W., Wu, K., Han, Y., 2016. Effects of steel properties on the local buckling response of high strength pipelines subjected to reverse faulting. J. Nat. Gas Sci. Eng. 33, 378–387.

Nair, G.S., Dash, S.R., Mondal, G., 2018. Review of pipeline performance during earthquakes since 1906. J. Perform. Constr. Facil. 32 (6), 1–18. https://doi.org/10.1061/(ASCE)CF.1943-5509.0001214.

O'Rourke, T.D., Bonneau, A., 2007. Lifeline Performance under Extreme Loading during Earthquakes. Earthquake Geotechnical Engineering. In: Pitilakis, K.D. (Ed.). Springer, Dordrecht, Netherlands, pp. 407–432.

Ovesen, N.K., 1981. Centrifuge tests of the uplift capacity of anchor'. In: Proc. Of the Tenth International Conference on Soil Mechanics and Foundation Engineering, Stockholm, pp. 712–722.

Ozcebe, A.G., Paolucci, R., Mariani, S., 2017. Numerical modeling of the interaction of pressurized large diameter gas buried pipelines with normal fault ruptures. Soil Dynam. Earthq. Eng. 101, 105–115.

Rayleigh, J.W.S.B., 1877. Theory of Sound, Volume II, London: Macmillan and Co.

Reilinger, R.E., Ergintav, S., Bürgmann, R., McClusky, S., Lenk, O., Barka, A., Gurkan, O., Hearn, L., Feigl, K.L., Cakmak, R., Aktug, B., Ozener, H., Töksoz, M.N., 2000. Coseismic and postseismic fault slip for the 17 August 1999, M = 7.5, Izmit, Turkey earthquake. Science 289 (5484), 1519–1524.

Sarvanis, G.C., Karamanos, S.A., 2017. Analytical model for the strain analysis of continuous buried pipelines in geohazard areas. Eng. Struct. 152, 57–69.

Schiff, A.J., 1988. The whittier narrows, California earthquake of october 1, 1987, response of lifelines and their effect on emergency response, the whittier narrows earthquake of october 1, 1987. Earthq. Spectra 4 (1), 339–366.

Sim, W.W., Towhata, I., Yamada, S., 2012. One-g shaking-table experiments on buried pipelines crossing a strike-slip fault. Geotechnique 62, 1067–1079. ISSN: 0016-8505.

Southern California Gas Company, 1973. Earthquake effects on southern California gas company facilities. San Fernando, California Earthquake of February 9, 1971 2, 59–66. U.S. Department of Commerce, Washington, D C.

Turner, J., 2004. Lateral Force–Displacement Behavior of Pipes in Partially Saturated Sand. MS thesis. School of Civil and Environmental Engineering, Cornell University, Ithaca, NY, p. 2004.

Vazouras, P., Karamanos, S.A., Dakoulas, P., 2010. Finite element analysis of buried steel pipelines under strike-slip fault displacement. Soil Dynam. Earthq. Eng. 30 (11), 1361–1376.

Vazouras, P., Karamanos, S.A., Dakoulas, P., 2012. Mechanical behavior of buried steel pipes crossing active strike-slip faults. Soil Dynam. Earthq. Eng. 41, 164–180.

Vazouras, P., Dakoulas, P., Karamanos, S.A., 2015. Pipe-soil interaction and pipeline performance under strike-slip fault movements. Soil Dynam. Earthq. Eng. 72, 48–65.

Zhang, L., Zhao, X., Yan, X., Yang, X., 2016. A new finite element model of buried steel pipelines crossing strike-slip faults considering equivalent boundary springs. Eng. Struct. 123, 30–44.